



# The great escape: Petrogenesis of low-silica volcanism of Pliocene to Quaternary age associated with the Altiplano-Puna Volcanic Complex of northern Chile (21°10'–22°50'S)

Oswaldo González-Maurel<sup>a,b,\*</sup>, Petrus le Roux<sup>b</sup>, Benigno Godoy<sup>c</sup>, Valentin R. Troll<sup>d,e</sup>, Frances M. Deegan<sup>d</sup>, Andrew Menzies<sup>f</sup>

<sup>a</sup> Departamento de Ciencias Geológicas, Universidad Católica del Norte, Avenida Angamos 0610, Antofagasta, Chile

<sup>b</sup> Department of Geological Sciences, University of Cape Town, Rondebosch 7700, South Africa

<sup>c</sup> Centro de Excelencia en Geotermia de los Andes (CEGA) y Departamento de Geología, Facultad de Ciencias Físicas y Matemáticas, Universidad de Chile, Plaza Ercilla 803, Santiago, Chile

<sup>d</sup> Department of Earth Sciences, Natural Resources and Sustainable Development, Uppsala University, SE-75236 Uppsala, Sweden

<sup>e</sup> Instituto de Estudios Ambientales y Recursos Naturales (i-UNAT), Departamento de Física (Geología), Universidad de Las Palmas de Gran Canaria, Spain

<sup>f</sup> Bruker Nano GmbH, Am Studio 2D, Berlin 12,489, Germany

## ARTICLE INFO

### Article history:

Received 4 June 2019

Received in revised form 30 July 2019

Accepted 31 July 2019

Available online 05 August 2019

### Keywords:

Low-silica volcanism

Altiplano-Puna Volcanic Complex

Altiplano-Puna Magma Body

Sr and Nd radiogenic isotopes

## ABSTRACT

The Pliocene to Quaternary volcanic arc of the Central Andes formed on 70–74 km thick continental crust. Physical interaction between mafic and acid magmas for this arc are therefore difficult to recognize due to the differentiation of mantle-derived magma during ascent through the thickened crust and a corresponding lack of erupted primitive lavas. However, a rare concentration of less evolved rocks is located marginal to the partially molten Altiplano-Puna Magma Body (APMB) in the Altiplano-Puna Volcanic Complex of northern Chile, between 21°10'S and 22°50'S. To unravel the relationship between this less evolved magmatism and the APMB, we present major and trace element data, and Sr and Nd isotope ratios of fourteen volcanoes. Whole-rock compositional and Sr and Nd isotope data reveal a large degree for compositional heterogeneity, e.g., SiO<sub>2</sub> = 53.2 to 63.2 wt%, MgO = 1.74 to 6.08 wt%, Cr = 2 to 382 ppm, Sr = 304 to 885 ppm, <sup>87</sup>Sr/<sup>86</sup>Sr = 0.7055 to 0.7088, and <sup>143</sup>Nd/<sup>144</sup>Nd = 0.5122 to 0.5125. The combined dataset points to magma spatial compositional changes resulting from magma mixing, fractional crystallization and crustal assimilation. The least evolved products erupted along the periphery of the APMB and are likely equivalent to the replenishing magmas that thermally sustain the large APMB system. We suggest that the mafic to intermediate eruptives we have investigated reflect mafic melt injections that underplate the APMB and escape along the side of the large felsic body to avoid significant compositional modifications during ascent, which helps to assess the evolution of the APMB through space and time.

© 2019 Elsevier B.V. All rights reserved.

## 1. Introduction

The Pliocene to Quaternary volcanic arc of the Central Andes is spread over southern Peru, western Bolivia, northwestern Argentina and northern Chile (14°S–28°S) and developed on the world's thickest continental arc crust (70–74 km; Beck et al., 1996; Fig. 1). Several authors have identified a wide compositional range for the Pliocene to Quaternary volcanic rocks in this region and most of the erupted materials are andesitic to dacitic in composition, usually displaying high-K calc-alkaline trends

and a strong subduction signature (e.g. Mamani et al., 2010; Wörner et al., 2018). Most magmas in the region have high <sup>87</sup>Sr/<sup>86</sup>Sr (> 0.706) and low <sup>143</sup>Nd/<sup>144</sup>Nd (< 0.5125) ratios relative to primitive mantle-type magmas (i.e. <sup>87</sup>Sr/<sup>86</sup>Sr = 0.703, Harmon et al., 1981; <sup>143</sup>Nd/<sup>144</sup>Nd > 0.5129, Davidson et al., 1991) and several authors have thus argued for compositional modification of parental magma by fractional crystallization and assimilation during ascent through the thickened Andean crust (Davidson et al., 1991; Francis and Hawkesworth, 1994; Mamani et al., 2010). Accordingly, primitive (parental) mafic compositions are rare, with olivine and pyroxene phyric basaltic-andesite to andesite rocks (commonly referred as “mafic”) representing the most primitive volcanic products in the region (Fig. 1; e.g. Davidson et al., 1990; Drew et al., 2009). The mafic volcanism within the

\* Corresponding author at: Departamento de Ciencias Geológicas, Universidad Católica del Norte, Avenida Angamos 0610, Antofagasta, Chile, and Department of Geological Sciences, University of Cape Town, Rondebosch 7700, South Africa.

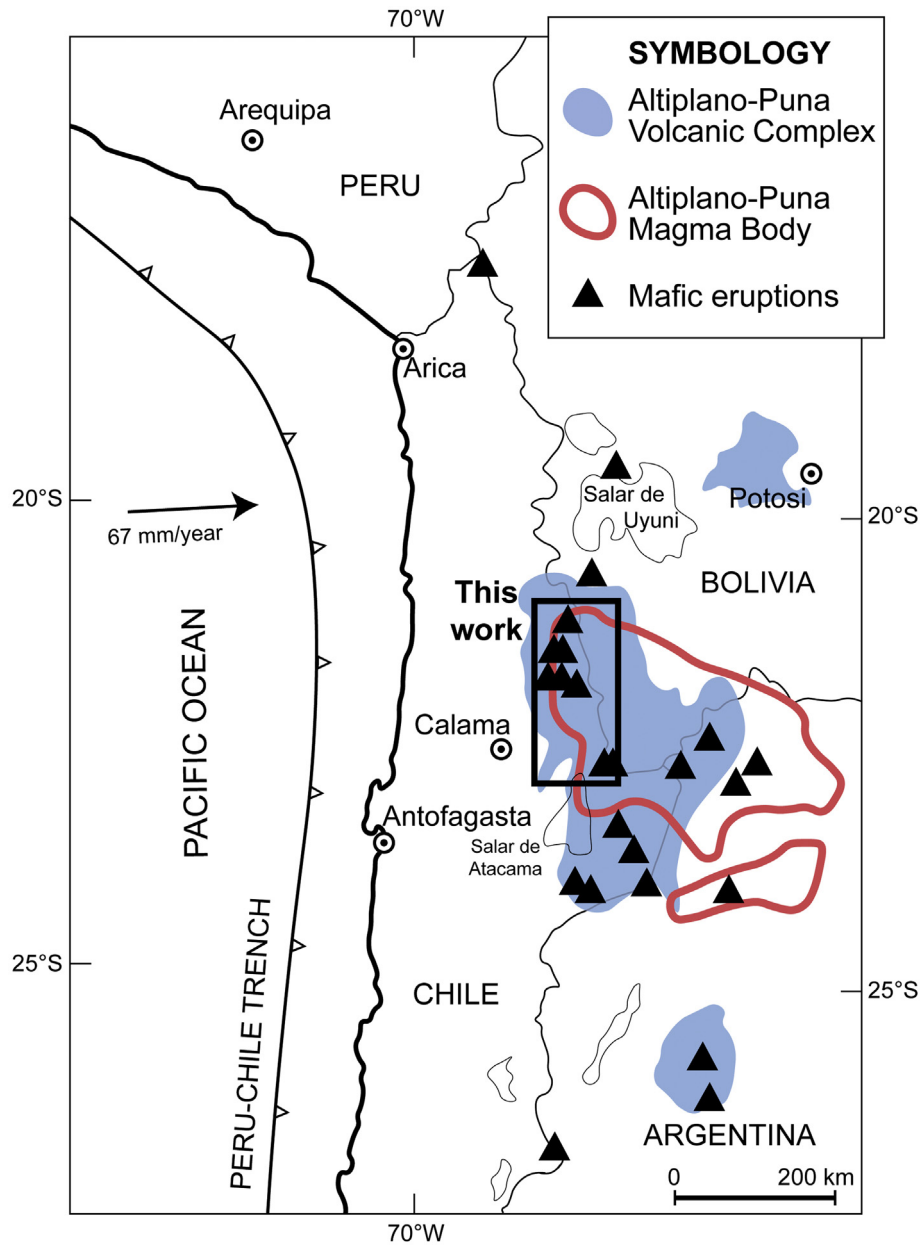


**Fig. 1.** Map of the Pliocene to Quaternary arc of the Central Andes showing the location of mafic erupted materials (black triangles) relative to the Altiplano-Puna Volcanic Complex (APVC) and Altiplano-Puna Magma Body (APMB) partial melt anomaly. The distribution of the APVC and the surface projection of APMB are based on Zandt et al. (2003).

modern arc has been studied in some detail (e.g. Burns et al., 2015; González-Maurel et al., 2019; Mattioli et al., 2006) and is considered the result of primitive mantle wedge melts having assimilated crustal material at high pressures during deep MASH-type processes (de Silva and Kay, 2018; Hildreth and Moorbath, 1988; Wörner et al., 2018).

Modern volcanic activity generally produced stratovolcanoes and few monogenetic volcanoes but also extensive ignimbrite deposits (Mamani et al., 2010). The volcano-tectonic ignimbrite province of the Altiplano-Puna Volcanic Complex (APVC, de Silva, 1989; Fig. 1) covers a surface area >70,000 km<sup>2</sup>, constituting one of the largest ignimbrite provinces in the world. Within this province, the scarce mafic magmatism has been interpreted as a result of direct, and possibly rapid, ascent of a superheated hydrous

basaltic magma from the mantle as a result of extensional tectonics and crustal relaxation (Mattioli et al., 2006). Alternatively, some authors have suggested that the presence of slightly more evolved mafic magmatism within the APVC may be related to interaction between ascending mafic magmas and the partially molten crustal material of the large-volume felsic Altiplano-Puna Magma Body (APMB; Godoy et al., 2017; González-Maurel et al., 2019), whose surface projection overlaps with the APVC distribution (Fig. 1). However, a concentration of mafic to intermediate, olivine-pyroxene-rich lavas erupted within the western border of the Altiplano-Puna volcanic region in northern Chile, i.e. between 21°10'S and 22°50'S (Fig. 1), from Pliocene to Quaternary stratovolcanoes and monogenetic cones (e.g. Godoy et al., 2019; González-Maurel et al., 2019; Sellés and Gardeweg, 2017; Taussi

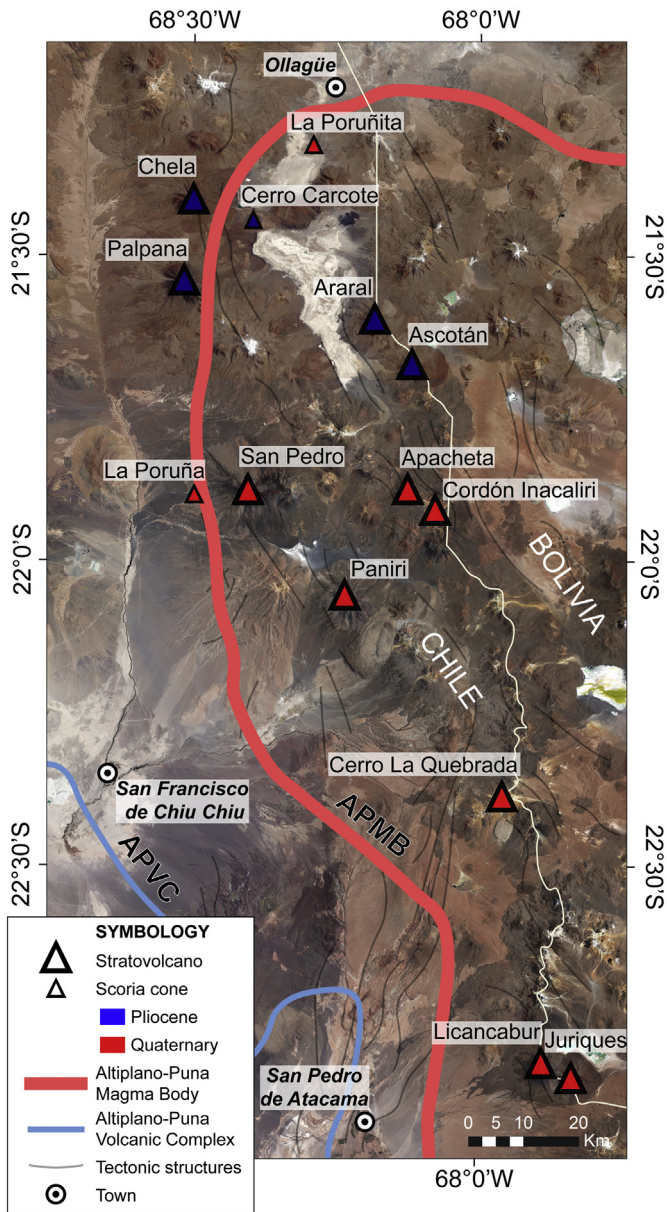


**Fig. 2.** Satellite image (Google Earth™) showing the location of the Pliocene and Quaternary volcanoes included in this study. The distribution of the APVC and the surface projection of the APMB are based on Zandt et al. (2003). Pliocene to Quaternary tectonic structures based on Giambiagi et al. (2016), Sellés and Gardeweg (2017) and Tibaldi et al. (2017).

et al., 2019). In this paper, we present new petrography, geochemistry and radiogenic isotope data to evaluate the petrogenesis of these olivine and/or pyroxene phyrlic mafic to intermediate rocks and assess their spatiotemporal relationship with the evolved APMB with the goal to evaluate the nature of the parental magmas in the region and to unravel evolutionary processes during storage and ascent through the crust.

## 2. Geological background

The Altiplano-Puna Magmatic Body (APMB, Chmielowski et al., 1999; Fig. 1) is a region of partially molten material in the upper crust, at 4 to 30 km depth, defined by electrical conductivity,

thermal and seismic anomalies (e.g. Araya Vargas et al., 2019; Ward et al., 2014; Zandt et al., 2003). The fraction of partial melt in the upper APMB is thought to exceed 20 vol% (Comeau et al., 2015; Ward et al., 2014), resulting from large-scale heat advection related to stagnation of mantle-derived mafic magmas (de Silva and Gosnold, 2007; del Potro et al., 2013). The surface projection of the Altiplano-Puna partial melting zone (i.e. APMB) is reflected on the surface by the Altiplano-Puna Volcanic Complex (APVC, de Silva, 1989), which is characterized by the presence of massive Miocene to Pleistocene high-silica ignimbrite sheets that are concentrated in the Western Cordillera, southern Altiplano and northern Puna between 21° and 24°S (Fig. 1; de Silva, 1989). The APMB is thus considered as the source region of the APVC ignimbrites (Zandt et al., 2003), which were likely generated by mafic magmas and anatectic melts of the upper crust that accumulated at 5 to 10 km depth (e.g. Freymuth et al., 2015; Kay et al., 2010; Kern et al., 2016). In addition to this regional scale ignimbritic activity, occasional mafic magma eruptions have been recognized around the margins of the APMB in the form of lava flows erupted from Miocene to Quaternary stratovolcano complexes and scoria cones (Fig. 1; e.g. Davidson and de Silva, 1995; Godoy et al., 2019; González-Maurel et al., 2019). The mafic to intermediate volcanism in the Chilean Western Cordillera (between 21°10'S and 22°50'S) has been sampled from fourteen volcanoes with olivine and/or pyroxene-rich rocks among their erupted materials (Fig. 2), comprising volcanic activity at Araral, Ascotán, Cerro Carcote, Chela and Palpana volcanoes during the Pliocene (Table 1; Fig. 2), and Apacheta, Cerro La Quebrada, Cordón Inacaliri, Juriques, Licancabur, La Poruña, La Poruña, Paniri and San Pedro volcanoes during the Quaternary (Table 1; Fig. 2). Several volcanoes occur in NW-SE trending alignments (i.e. Araral-Ascotán, San Pedro-Paniri, Apacheta-Cordón Inacaliri, Licancabur-Juriques), which are parallel to principal local tectonic structures in the region (Fig. 2; Giambiagi et al., 2016; Sellés and Gardeweg, 2017; Tibaldi et al., 2017), whereas others appear clustered (i.e. Chela-Palpana-Cerro Carcote; San Pedro-La Poruña; Fig. 2).

## 3. Analytical methods

To fully characterise the olivine and/or pyroxene-rich rocks erupted in the Chilean Western Cordillera, we present new petrography (Table 2), whole-rock major element, trace element and radiogenic isotope data of forty-eight (48) fresh volcanic rock samples (Supplementary Material 1; Table S1) from Pliocene to Quaternary lava flows from Central Andean stratovolcanoes and scoria cones (Fig. 2).

All 48 samples were crushed and pulverized at the Department of Geological Sciences, University of Cape Town (South Africa). Major and trace elemental abundance and isotope measurements were performed at UCT and detailed sample preparation procedures and standard values, as well as equipment descriptions for the analytical methods were as presented previously in Supplementary Material 3 of González-Maurel et al. (2019). Bulk-rock major element compositions were obtained by X-ray fluorescence spectrometry (XRF) using a Panalytical Axios wavelength dispersive XRF spectrometer following the procedures, standards and parameters outlined in González-Maurel et al. (2019) (see also Frimmel et al., 2001). A ThermoFisher Xseries II inductively coupled plasma mass spectrometer (ICP-MS) was used to obtain bulk trace element data by analysis of sample solutions using the methodology in Harris et al. (2015). A Nu Instruments NuPlasma HR multi-collector inductively couple plasma mass spectrometer (MC-ICP-MS) equipped with a DSN-100 desolvating nebulizer

**Table 1**  
Summarized K–Ar,  $^{40}\text{Ar}/^{39}\text{Ar}$ , U–Pb and relative published dating for the Pliocene and Quaternary studied volcanoes at  $21^{\circ}10'S$  to  $22^{\circ}50'S$ .

Volcano	Sample	Latitude (S)	Longitude (W)	Age (Ma)	Uncertainty ( $2\sigma$ )	Method	Reference	
<i>Pliocene</i>								
Chela	CHE 08	$21^{\circ} 24' 20''$	$68^{\circ} 27' 0''$	4.11	0.25	K–Ar (whole-rock)	Wörner et al. (2000)	
	CHE 07	$21^{\circ} 25' 30''$	$68^{\circ} 25' 50''$	3.75	0.5	K–Ar (whole-rock)	Wörner et al. (2000)	
Palpana	PAL 04	$21^{\circ} 34' 0''$	$68^{\circ} 29' 40''$	3.81	0.3	K–Ar (whole-rock)	Wörner et al. (2000)	
	PAL 01	$21^{\circ} 33' 55''$	$68^{\circ} 29' 55''$	3.65	0.15	K–Ar (whole-rock)	Wörner et al. (2000)	
Cerro Carcote	CAR 01	$21^{\circ} 26' 10''$	$68^{\circ} 23' 10''$	3.34	0.3	K–Ar (whole-rock)	Wörner et al. (2000)	
	CAR 01	$21^{\circ} 26' 10''$	$68^{\circ} 23' 10''$	2.82	0.11	K–Ar (whole-rock)	Wörner et al. (2000)	
Araral	AI-040	$21^{\circ} 35' 29''$	$68^{\circ} 14' 3''$	2.75	0.04	$^{40}\text{Ar}/^{39}\text{Ar}$ (amphibole)	Sellés and Gardeweg (2017)	
Ascotán	AI-053	$21^{\circ} 42' 18''$	$68^{\circ} 11' 4''$	2.67	0.02	$^{40}\text{Ar}/^{39}\text{Ar}$ (groundmass)	Sellés and Gardeweg (2017)	
<i>Quaternary</i>								
Cordón Inacaliri	AI-226	$21^{\circ} 51' 22''$	$68^{\circ} 6' 52''$	1.43	0.02	$^{40}\text{Ar}/^{39}\text{Ar}$ (groundmass)	Sellés and Gardeweg (2017)	
	AI-201	$21^{\circ} 55' 28''$	$68^{\circ} 10' 1''$	1.109	0.023	$^{40}\text{Ar}/^{39}\text{Ar}$ (groundmass)	Sellés and Gardeweg (2017)	
	AI-256	$21^{\circ} 56' 1''$	$68^{\circ} 5' 9''$	1.094	0.016	$^{40}\text{Ar}/^{39}\text{Ar}$ (groundmass)	Sellés and Gardeweg (2017)	
Cerro La Quebrada	M2	$22^{\circ} 24' 52''$	$67^{\circ} 57' 10''$	0.9	–	U–Pb (zircon)	Bidart (2014)	
Licancabur	–	–	–	> 1.35	–	Relative	Figuroa et al. (2009)	
Juriques	–	–	–	> 1.35	–	Relative	Marinovic and Lahsen (1984)	
Paniri	PAE-090	$22^{\circ} 0' 0''$	$68^{\circ} 14' 8''$	1.39	0.29	$^{40}\text{Ar}/^{39}\text{Ar}$ (amphibole)	Godoy et al. (2017)	
	PAE-55	$22^{\circ} 3' 45''$	$68^{\circ} 11' 24''$	0.64	0.14	$^{40}\text{Ar}/^{39}\text{Ar}$ (amphibole)	Godoy et al. (2017)	
	PAE-43	$22^{\circ} 7' 55''$	$68^{\circ} 15' 16''$	0.625	0.093	$^{40}\text{Ar}/^{39}\text{Ar}$ (amphibole)	Godoy et al. (2017)	
	ZZ-27a	$22^{\circ} 8' 30''$	$68^{\circ} 16' 3''$	0.5	0.1	K–Ar (whole-rock)	Seelenfreund et al. (2009)	
	ZZ-46	$22^{\circ} 8' 30''$	$68^{\circ} 16' 3''$	0.4	0.1	K–Ar (whole-rock)	Seelenfreund et al. (2009)	
	PAE-03	$22^{\circ} 2' 50''$	$68^{\circ} 12' 29''$	0.325	0.008	$^{40}\text{Ar}/^{39}\text{Ar}$ (groundmass)	Godoy et al. (2017)	
	ZZ-42	$22^{\circ} 5' 19''$	$68^{\circ} 11' 48''$	0.3	0.1	K–Ar (whole-rock)	Seelenfreund et al. (2009)	
	PAE-02	$22^{\circ} 2' 47''$	$68^{\circ} 12' 35''$	0.264	0.099	$^{40}\text{Ar}/^{39}\text{Ar}$ (amphibole)	Godoy et al. (2017)	
	PAE-25	$22^{\circ} 3' 44''$	$68^{\circ} 15' 31''$	0.164	0.003	$^{40}\text{Ar}/^{39}\text{Ar}$ (groundmass)	Godoy et al. (2017)	
	PAE-08	$22^{\circ} 6' 13''$	$68^{\circ} 17' 49''$	0.15	0.006	$^{40}\text{Ar}/^{39}\text{Ar}$ (amphibole)	Godoy et al. (2017)	
	Apacheta	AA-067	$21^{\circ} 51' 0''$	$68^{\circ} 12' 40''$	0.97	0.11	$^{40}\text{Ar}/^{39}\text{Ar}$ (groundmass)	Taussi et al. (2019)
La Poruñita	PORU 02	$21^{\circ} 17' 40''$	$68^{\circ} 15' 35''$	0.68	0.2	K–Ar (whole-rock)	Wörner et al. (2000)	
	PORU 02	$21^{\circ} 17' 40''$	$68^{\circ} 15' 35''$	0.65	0.2	K–Ar (whole-rock)	Wörner et al. (2000)	
	PORU 02 (bomb)	$21^{\circ} 17' 40''$	$68^{\circ} 15' 35''$	0.42	0.2	K–Ar (whole-rock)	Wörner et al. (2000)	
San Pedro	DB251114-5	$21^{\circ} 49' 5''$	$68^{\circ} 23' 10''$	0.166	0.012	$^{40}\text{Ar}/^{39}\text{Ar}$ (groundmass)	Bertin and Amigo (2019)	
	DB190714-1	$21^{\circ} 54' 28''$	$68^{\circ} 22' 0''$	0.166	0.016	$^{40}\text{Ar}/^{39}\text{Ar}$ (groundmass)	Bertin and Amigo (2019)	
	DB060911-2	$21^{\circ} 54' 15''$	$68^{\circ} 29' 2''$	0.160	0.050	$^{40}\text{Ar}/^{39}\text{Ar}$ (groundmass)	Bertin and Amigo (2019)	
	DB170714-2	$21^{\circ} 57' 22''$	$68^{\circ} 23' 6''$	0.159	0.003	$^{40}\text{Ar}/^{39}\text{Ar}$ (groundmass)	Bertin and Amigo (2019)	
	DB060911-3	$21^{\circ} 53' 58''$	$68^{\circ} 28' 11''$	0.140	0.040	$^{40}\text{Ar}/^{39}\text{Ar}$ (groundmass)	Bertin and Amigo (2019)	
	DB251114-4	$21^{\circ} 52' 21''$	$68^{\circ} 23' 59''$	0.139	0.033	$^{40}\text{Ar}/^{39}\text{Ar}$ (groundmass)	Bertin and Amigo (2019)	
	GO060911-1	$21^{\circ} 49' 29''$	$68^{\circ} 27' 59''$	0.130	0.040	$^{40}\text{Ar}/^{39}\text{Ar}$ (amphibole)	Bertin and Amigo (2019)	
	SP12-02A	$21^{\circ} 56' 4''$	$68^{\circ} 30' 36''$	0.107	0.012	$^{40}\text{Ar}/^{39}\text{Ar}$ (groundmass)	Delunel et al. (2016)	
	DB140613-3	$21^{\circ} 51' 42''$	$68^{\circ} 29' 55''$	0.097	0.014	$^{40}\text{Ar}/^{39}\text{Ar}$ (groundmass)	Bertin and Amigo (2019)	
	DB200714-2B	$21^{\circ} 57' 41''$	$68^{\circ} 27' 24''$	0.096	0.036	$^{40}\text{Ar}/^{39}\text{Ar}$ (groundmass)	Bertin and Amigo (2019)	
	SPSP 16 01	$21^{\circ} 51' 13''$	$68^{\circ} 27' 12''$	0.096	0.008	$^{40}\text{Ar}/^{39}\text{Ar}$ (groundmass)	González-Maurel et al. (2019)	
	DB060911-4	$21^{\circ} 52' 23''$	$68^{\circ} 29' 15''$	0.090	0.080	$^{40}\text{Ar}/^{39}\text{Ar}$ (groundmass)	Bertin and Amigo (2019)	
	DB200714-2C	$21^{\circ} 57' 41''$	$68^{\circ} 27' 24''$	0.068	0.027	$^{40}\text{Ar}/^{39}\text{Ar}$ (groundmass)	Bertin and Amigo (2019)	
	DB140613-2	$21^{\circ} 50' 26''$	$68^{\circ} 30' 18''$	0.060	0.006	$^{40}\text{Ar}/^{39}\text{Ar}$ (groundmass)	Bertin and Amigo (2019)	
	La Poruña	POR 15 05	$21^{\circ} 55' 32''$	$68^{\circ} 34' 2''$	0.11	0.011	$^{40}\text{Ar}/^{39}\text{Ar}$ (groundmass)	González-Maurel et al. (2019)
		DB120613-2	$21^{\circ} 54' 13''$	$68^{\circ} 30' 52''$	0.11	0.05	$^{40}\text{Ar}/^{39}\text{Ar}$ (whole-rock)	Bertin and Amigo (2019)
		POR 15 04	$21^{\circ} 53' 35''$	$68^{\circ} 30' 19''$	0.092	0.034	$^{40}\text{Ar}/^{39}\text{Ar}$ (groundmass)	González-Maurel et al. (2019)

was used for Sr and Nd isotope analyses. Full details of the isotope analysis method were published by Harris et al. (2015). Typical internal two-sigma analytical errors for individual analyses were < 2%RSD for XRF, < 3%RSD for ICP-MS, and < 0.003%RSD for  $^{87}\text{Sr}/^{86}\text{Sr}$  and  $^{143}\text{Nd}/^{144}\text{Nd}$  ratios (González-Maurel et al., 2019). The accuracy and precision of these analytical data presented in this study are indicated by Table S2.1 in Supplementary Material 2 of this paper, where similar to Table S3.1 of González-Maurel et al. (2019) results for analysis of reference material JA-2 and averages of repeat analysis of three samples from this study are listed.

## 4. Results

### 4.1. Petrography and mineral assemblage

With respect to mineralogy, the petrographic description follows a definition of phenocrysts = 0.2–2.5 mm, microcrysts =

0.2–0.03 mm and microlite  $\leq 0.03$  mm. Most of the olivine and/or pyroxene-rich rock samples are dark-coloured, fine-grained and porphyritic. The phenocrysts (up to 40 vol%) comprise plagioclase, orthopyroxene, clinopyroxene and olivine. Amphibole and biotite occur only rarely as microcrysts and/or microlites. Phenocrysts and microcrysts are generally suspended in a very finely crystalline groundmass with interstitial glass and microlites of, in order of decreasing abundance, plagioclase, pyroxene, olivine, amphibole and Fe–Ti oxides. A hypocrySTALLINE texture is common in many of the rocks, however glassy lavas can also be found. Groundmass varies from compact to vesicular. Although vesicular rocks are not common, vesicularity is high (> 40 vol%) in scoria samples from La Poruña, La Poruñita and San Pedro. Three Pliocene samples from Cerro Carcote, Chela and Palpana have a reddish-brown groundmass colour, due to the presence of very fine-grained hydrothermal alteration minerals (e.g. illite, anhydrite, K-rich clays). Secondary quartz was observed in a few

**Table 2**

Petrography and phenocryst main assemblages of the studied Pliocene to Quaternary volcanism at 21°10'S to 22°50'S. Geochemical data from Table S1.

Volcano	Sample	SiO <sub>2</sub> (wt%) <sup>a</sup>	Chemical classification <sup>a</sup>	Rock type	Mineral assemblage
<b>Olivine-pyroxene-bearing rocks</b>					
<i>Pliocene</i>					
Araral	ARA-01	63.04	Andesite	Glassy fine-grained plg-ol-px seriate glomerophyric	plg > opx = cpx > ol
	ARA-04	61.15	Andesite	Glassy fine-grained plg-ol-px seriate glomerophyric	plg > opx = cpx > ol
	ARA-10	62.29	Andesite	Glassy fine-grained plg-ol-px seriate glomerophyric	plg > opx = cpx > ol
Cerro Carcote	CAR-01	57.07	Basaltic trachyandesite	Fine-grained ol-px phyric	plg (only microlite) > ol > opx = cpx
	CAR-03	59.42	Trachyandesite	Fine-grained ol-px phyric	plg (only microlite) > opx > ol > cpx
	CAR-04	56.03	Basaltic trachyandesite	Vesicular fine-grained ol-cpx phyric	plg (only microlite) > cpx > ol > opx
Chela	CHE-01	57.92	Basaltic-andesite	Fine-grained ol-cpx phyric	plg (only microlite) > ol > cpx > opx
	CHE-02	56.68	Basaltic-andesite	Fine-grained plg-ol-px seriate phyric	plg > opx = cpx > ol
	CHE-03	55.50	Basaltic-andesite	Fine-grained plg-ol seriate phyric px glomerophyric	plg > ol > cpx > opx
	CHE-04	57.30	Basaltic-andesite	Fine-grained plg-px seriate phyric	plg > opx = cpx > ol
	CHE-05	58.75	Andesite	Fine-grained plg-px seriate phyric	plg > opx = cpx > ol
Palpana	PAL-02	58.36	Andesite	Fine-grained plg-px seriate phyric	plg > cpx > opx > ol
	PAL-03	59.48	Trachyandesite	Fine-grained plg-px seriate phyric	plg > cpx > opx > ol
<i>Quaternary</i>					
C. La Quebrada	QUE-01	58.87	Andesite	Vesicular glassy fine-grained plg-ol seriate phyric	plg > ol > opx = cpx
Juriques	JUR-05	53.70	Basaltic-andesite	Fine-grained plg-ol seriate phyric px glomerophyric	plg > opx = cpx > ol
La Poruñita	POR-01	57.47	Basaltic-andesite	Vesicular fine-grained plg-ol-px seriate phyric	plg > ol > opx = cpx
	POR-02	57.46	Basaltic-andesite	Vesicular fine-grained ol phyric plg-px glomerophyric	plg > ol > opx = cpx
	POR-03	57.48	Basaltic-andesite	Fine-grained plg-ol-px seriate phyric	plg > ol > opx = cpx
	POR-04	59.85	Andesite	Glassy fine-grained plg-ol-px seriate phyric	plg > ol > opx = cpx
	POR-05	59.21	Basaltic trachyandesite	Fine-grained plg-ol-cpx seriate phyric	plg > ol > cpx > opx
	POR-06	56.30	Basaltic-andesite	Glassy fine-grained plg-ol-px seriate phyric	plg > ol > cpx > opx
	POR-07	56.86	Basaltic-andesite	Glassy fine-grained plg-ol-px seriate phyric	plg > ol > cpx > opx
	POR-08	56.63	Basaltic-andesite	Fine-grained plg-ol-px seriate phyric	plg > ol > opx = cpx
	POR-09	57.51	Basaltic-andesite	Vesicular fine-grained plg-ol-px seriate phyric	plg > ol > opx > cpx
	POR-10	58.23	Andesite	Vesicular fine-grained plg-ol-px seriate phyric	plg > ol > opx = cpx
La Poruñita	PORU-01	56.56	Basaltic trachyandesite	Vesicular fine-grained ol-px phyric	plg (only microlite) > ol > opx = cpx
	PORU-02	56.72	Basaltic trachyandesite	Vesicular fine-grained ol-px phyric	plg (only microlite) > ol > opx = cpx
Paniri	PANI-03	57.74	Basaltic trachyandesite	Fine-grained ol phyric plg-opx glomerophyric	plg > ol = opx > cpx
	PANI-05	57.04	Basaltic-andesite	Fine-grained plg phyric ol-px glomerophyric	plg > ol = opx = cpx
San Pedro	SPE-01	58.31	Andesite	Vesicular fine-grained plg-ol-px seriate phyric	plg > opx = cpx > ol
	SPE-09	56.60	Basaltic-andesite	Vesicular fine-grained plg-ol-px phyric	plg > ol > opx = cpx
	SPE-10	56.29	Basaltic-andesite	Vesicular fine-grained plg-ol-px phyric	plg > ol > cpx > opx
<b>Pyroxene-bearing rocks</b>					
<i>Pliocene</i>					
Ascotán	ASC-01	64.46	Dacite	Glassy fine-grained plg-px seriate glomerophyric	plg > opx > cpx
	ASC-04	64.78	Dacite	Glassy fine-grained plg-px seriate glomerophyric	plg > opx > cpx
	ASC-06	62.88	Andesite	Glassy fine-grained plg-px seriate glomerophyric	plg > opx > cpx
Cerro Carcote	CAR-02	59.64	Trachyandesite	Fine-grained opx phyric	plg > opx > cpx
Palpana	PAL-01	62.02	Trachyandesite	Glassy fine-grained plg-px seriate phyric	plg > cpx > opx
<i>Quaternary</i>					
Apacheta	APA-01	57.30	Basaltic trachyandesite	Glassy fine-grained plg-px seriate phyric	plg > opx = cpx
	APA-02	61.27	Andesite	Glassy fine-grained plg-px-amp seriate phyric	plg > opx = cpx > amp
Cordón Inacaliri	INA-01	63.30	Trachyandesite	Glassy fine-grained plg-px phyric	plg > opx > cpx
Juriques	JUR-01	55.45	Basaltic-andesite	Fine-grained plg-opx seriate glomerophyric	plg > opx > cpx
Licancabur	LIC-01	58.99	Andesite	Glassy fine-grained plg-ox phyric	plg > ox > cpx > opx
	PANI-01	59.88	Andesite	Glassy fine-grained plg-px-ox seriate glomerophyric	plg > opx = cpx > ox
Paniri	PANI-14	59.33	Basaltic-andesite	Glassy fine-grained plg-px-ox phyric	plg > opx > ox
	PANI-15	57.14	Basaltic-andesite	Glassy fine-grained plg-px seriate phyric	plg > opx > cpx
	SAN-02	62.84	Trachyte	Glassy fine-grained plg-px seriate glomerophyric	plg > opx = cpx
San Pedro	SPE-07	56.38	Basaltic-andesite	Fine-grained plg-ol-px seriate glomerophyric	plg > opx = cpx

<sup>a</sup> Recalculated to 100% anhydrous.

samples, either as interstitial mineral grains or as vesicle infill (See Table 2).

Plagioclase is the most abundant phase (>50 vol%) and typically appears as euhedral to subhedral crystals, ranging in size from microlites to phenocrysts (<2.5 mm). Plagioclase displays a diversity of morphologies and textures, including equant and/or tabular crystals with sieve, resorption, or regrowth rims, frequently displaying seriate and/or normal zonation. In consideration of the ferromagnesian phenocryst phases, the samples are either (i) olivine-pyroxene-bearing or (ii) pyroxene-bearing. Photomicrographs of representative mineral assemblages are presented in Fig. 3.

Olivine-pyroxene-bearing rocks are the most common mafic volcanic type in our sample set (Fig. 3a) and are found at both Pliocene and Quaternary volcanoes (Table 2). These lavas differ however among each other in terms of their average crystal sizes and frequent seriate texture, ranging from very fine- to fine-grained. They contain dominantly olivine, orthopyroxene, clinopyroxene and plagioclase with minor amphibole, magnetite and ilmenite. The olivine crystals (up to 2 mm; <10 vol%) include subhedral and rare skeletal forms, frequently contain Fe-Ti oxide inclusions, and often display disequilibrium textures around their outer edges such as embayments and orthopyroxene microcrysts (Fig. 3a). Orthopyroxene is common as a pristine phenocryst (up to 1 mm)

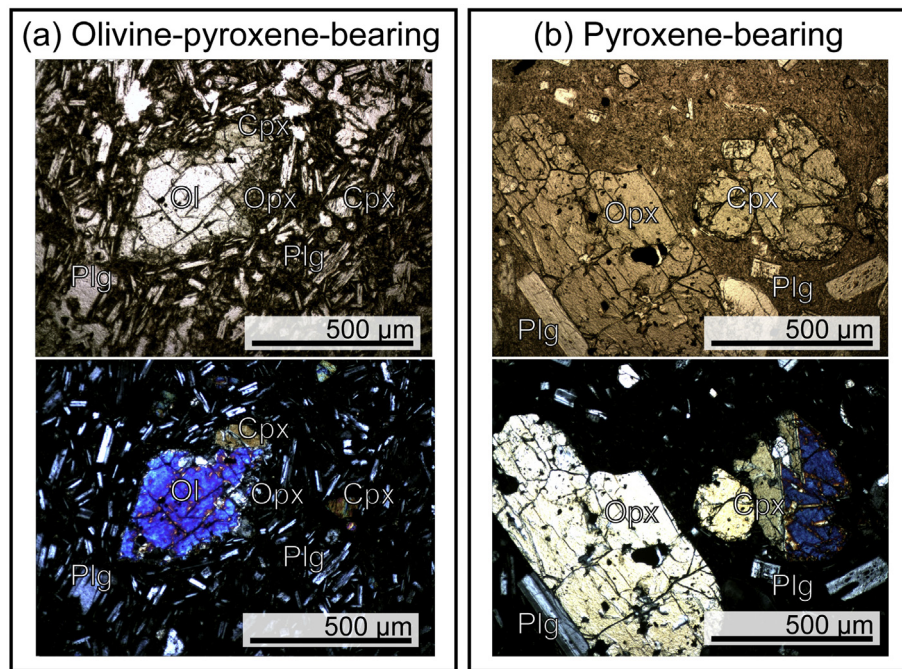


**Fig. 3.** Representative photomicrographs of the studied sample groups: (a) olivine-pyroxene-bearing and (b) pyroxene-bearing. Upper and lower panels show examples of plane-polarized light and cross-polarized light photomicrographs, respectively.

and microcryst (up to 0.2 mm) with usual abundance <20 vol%. Orthopyroxene crystals are euhedral to subhedral and occur individually or in small clusters with plagioclase and clinopyroxene. Clinopyroxene occurs as euhedral to subhedral crystals (up to 2 mm; < 15 vol%) or as reaction rims surrounding orthopyroxene phenocrysts and, similar to orthopyroxene, clinopyroxene crystals may occur individually or as glomerocrysts. A few samples contain olivine ± orthopyroxene or olivine ± clinopyroxene only, but plagioclase occurs as a phenocryst phase (up to 2.5 mm; < 40 vol%) in all but six olivine-pyroxene-bearing lavas from Cerro Carcote, Chela and La Poruña (Table 2).

Pyroxene-bearing lavas from individual volcanic centers show similar mineral assemblages (Fig. 3b), although optical microscope observations highlight some variability in modal mineralogy, texture, and grain size between different samples (Table 2). These lavas are very fine- to fine-grained (seriate texture) with variable phenocryst and microcryst abundances (> 5 to ca. 55 vol%). The most common assemblage is, in order of decreasing abundance, plagioclase, orthopyroxene, clinopyroxene as phenocrysts (Fig. 3b), with amphibole, olivine, Fe-Ti oxides as microcrysts. Alternatively, some samples show elongated amphibole (up to 1.2 mm; < 2 vol%) and/or magnetite ± ilmenite (0.2 to 0.7 mm; < 3 vol%) as phenocrysts. Orthopyroxene and/or clinopyroxene can also appear as minor phases. Plagioclase usually occurs as individual phenocrysts, up to 2.5 mm, (< 50 vol%) or in orthopyroxene-clinopyroxene-magnetite glomerocrysts. Orthopyroxene (up to 2 mm; < 15 vol%) and clinopyroxene (up to 2 mm; < 10 vol%) occur as subhedral to euhedral tabular crystals. Replacement of olivine by orthopyroxene or orthopyroxene by clinopyroxene is common around the phenocryst outer edges. Some pyroxenes show resorption features and/or Fe-Ti oxide inclusions. Crystals are then set in a glassy to hypocrySTALLINE groundmass with microlites of plagioclase, orthopyroxene, clinopyroxene, amphibole, magnetite, ilmenite

and olivine. These lavas are rather compact and show low vesicularity (< 10 vol%).

#### 4.2. Whole-rock geochemical and isotope composition

The full geochemical dataset of the samples from this study is provided in the Supplementary Material 1 (TableS1). The suite of samples comprises medium- to high-K calc-alkaline basaltic-andesites to dacites, with some rare basaltic-trachyandesite and trachyandesite compositions (Fig. 4). All studied rocks are subalkaline (Fig. 4a) and metaluminous in terms of the aluminum saturation index (molar A/CNK = 0.70–0.93; Zen, 1986). The variation of the major elements shows an increase in K<sub>2</sub>O (Fig. 4b) and a decrease in FeO\*, MnO and CaO with increasing silica, whereas Al<sub>2</sub>O<sub>3</sub>, Na<sub>2</sub>O and P<sub>2</sub>O<sub>5</sub> remain nearly constant.

The Pliocene lavas have a wide range of SiO<sub>2</sub> contents (SiO<sub>2</sub> = 54.6 to 63.2 wt%; Fig. 4), however most are classified as high Mg# lavas (44–57 Mg#; Kelemen et al., 2003). These samples show a well-defined negative trend of MgO against SiO<sub>2</sub> (Fig. 5a) and MgO correlates positively with Ni and Cr but scatters somewhat around 4 wt% MgO (Fig. 5b, c). Conversely, Sr shows no correlation with MgO (Fig. 5d). Quaternary lava samples (SiO<sub>2</sub> = 53.2 to 62.8 wt%; Fig. 4) classify as evolved, high Mg# and primitive lavas (Kelemen et al., 2003), ranging from 35 to 62 Mg#. These samples reveal the same correlations between silica and compatible trace elements with respect to MgO as seen in the Pliocene samples (Fig. 5).

All samples are enriched in large ion lithophile elements (LILE) relative to high field strength element (HFSE) normalized to primitive mantle concentrations (McDonough and Sun, 1995; Fig. 6a), consistent with typical continental arc compositions. The primitive mantle-normalized multi-element diagram (Fig. 6a) exhibits a pronounced negative Nb-Ta anomaly, a positive anomaly in Sr, K and

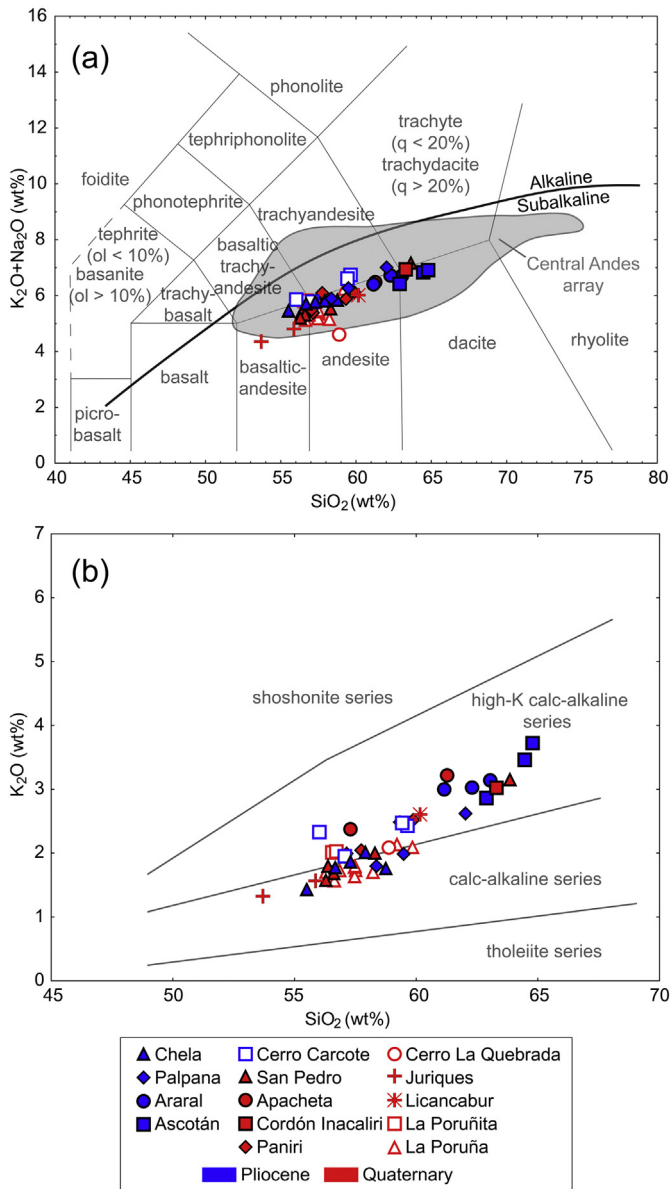


**Fig. 4.** (a) TAS diagram (Le Maitre et al., 1989) for volcanic rocks from the studied volcanoes. Solid line discriminates between alkaline and subalkaline rocks (Irvine and Baragar, 1971). Grey field represents the Central Andes array (Mamani et al., 2010). (b)  $K_2O$  vs.  $SiO_2$  classification diagram after Peccerillo and Taylor (1976).

Pb, and enrichment in Rb, Th and U. Chondrite-normalized rare earth element (REE; McDonough and Sun, 1995) patterns of the studied rock samples are enriched in light REE (LREE) relative to the depleted heavy REE (HREE) ( $La/Yb_N = 4.28–19.13$ ; Fig. 6b). A weak negative Eu anomaly ( $Eu/Eu^* = 0.65–0.91$ ) characterizes all studied samples (Fig. 6b).

The  $^{87}Sr/^{86}Sr$  and  $^{143}Nd/^{144}Nd$  ratios range from 0.705541 to 0.708746, and 0.512208 to 0.512513, respectively. From the Sr–Nd isotope diagram (Fig. 7), a pronounced negative correlation is observed, with a few samples showing scattered  $^{143}Nd/^{144}Nd$  ratios with respect to Sr isotope ratios at ca. 0.7065. Nd isotope ratios from the Quaternary rocks have a relatively restricted range compared to the variability revealed for the Pliocene samples (Fig. 7). The correlation of Sr and Nd isotope ratios with respect to silica and Sr contents reveal well-defined differentiation trends

for Pliocene lavas, whereas Quaternary rocks show an overall scattered distribution (Fig. 8).

## 5. Discussion

### 5.1. Magmatic differentiation processes and temporal variations

The major and trace element compositions define a strong subduction-related arc signature, typical for lavas in the Central Andes (e.g. Davidson et al., 1991; Hildreth and Moorbath, 1988; Mamani et al., 2010). There is a large variation in the Th–U concentrations of the samples (Fig. 6a) that is heavily influenced by different degrees of differentiation in the continental crust as the most differentiated samples ( $> 60$  wt%  $SiO_2$ ) show the higher Th and U concentrations (e.g. Fig. 9a). The overall REE element character of the samples generally resembles the basaltic-andesite end-member proposed by Blum-Oeste and Wörner (2016) (Fig. 6b), suggested to reflect an originally asthenospheric mantle source for the studied rocks. Their  $^{87}Sr/^{86}Sr$  and  $^{143}Nd/^{144}Nd$  ratios overlap consistently with the overall Central Andes array (Fig. 7). Petrographic descriptions reveal a relative homogeneity of mineral assemblages of (in order of decreasing abundance) plagioclase, orthopyroxene, clinopyroxene and olivine (Fig. 3; Table 2) and plagioclase, orthopyroxene and clinopyroxene crystal morphologies suggest they are usually in equilibrium with the host magma. The negative correlation between  $Eu/Eu^*$  and  $SiO_2$  (Fig. 9b) and positive trends of CaO, FeO, Cr and Ni with regard to MgO (Fig. 5) are consistent with fractional crystallization of the mineral assemblages observed in the samples (plagioclase + pyroxene ± olivine; Fig. 3) (McKay, 1989; Taylor and McLennan, 1988). However, disequilibrium textures in plagioclase (i.e. sieve textures) and in pyroxene (i.e. resorption features) are locally present and embayments are relatively common in olivine (Fig. 3). Embayments and orthopyroxene corona rims on olivine crystals (Fig. 3a) indicate chemical and thermal disequilibrium between the crystals and the melt (Streck, 2008), probably caused by the reaction of early formed olivine with  $SiO_2$  in the melt.

The most widely accepted generation model for basaltic-andesite arc magmas in the Central Andes comprises a lower crustal MASH (Melting-Assimilation-Storage-Homogenization) zone at ca. 70 km crustal depth where mantle-derived magmas stagnate and mix and homogenise with lower crustal melts (e.g. Davidson et al., 1991; Hildreth and Moorbath, 1988; Wörner et al., 2018). The Sr and Nd isotope data presented here reveal large isotopic variation even in the basaltic-andesite melts (Figs. 7 and 8), and some individual volcanoes demonstrate that further differentiation of such basaltic-andesite melts has been caused by coupled fractionation and assimilation of the continental crust (AFC, DePaolo, 1981; e.g. Cerro Carcote, Chela, Palpana), or by mixing with evolved contaminated melt (i.e. APMB) in the magma reservoir (e.g. Ascotán, Juriques, Paniri) (Fig. 8a, b). The occurrences of relatively low silica lavas with high Sr isotope ratios (Fig. 8a; e.g. La Poruña, San Pedro) can possibly be explained by selective assimilation of partial melts and low-temperature melting components, e.g. as a consequence of selective incorporation of evolved crustal components or partial crustal melts into the rising mafic magmas (e.g. González-Maurel et al., 2019; Meade et al., 2014; Troll et al., 2005). Most samples have depleted Sr/Y ratios compared with the Central Andean array (Fig. 9c), although they reflect that the differentiation processes were likely controlled by either mid ( $Sr/Y > 30$ ) and/or shallow crustal sources ( $Sr/Y < 30$ ). The relatively flat slopes for the

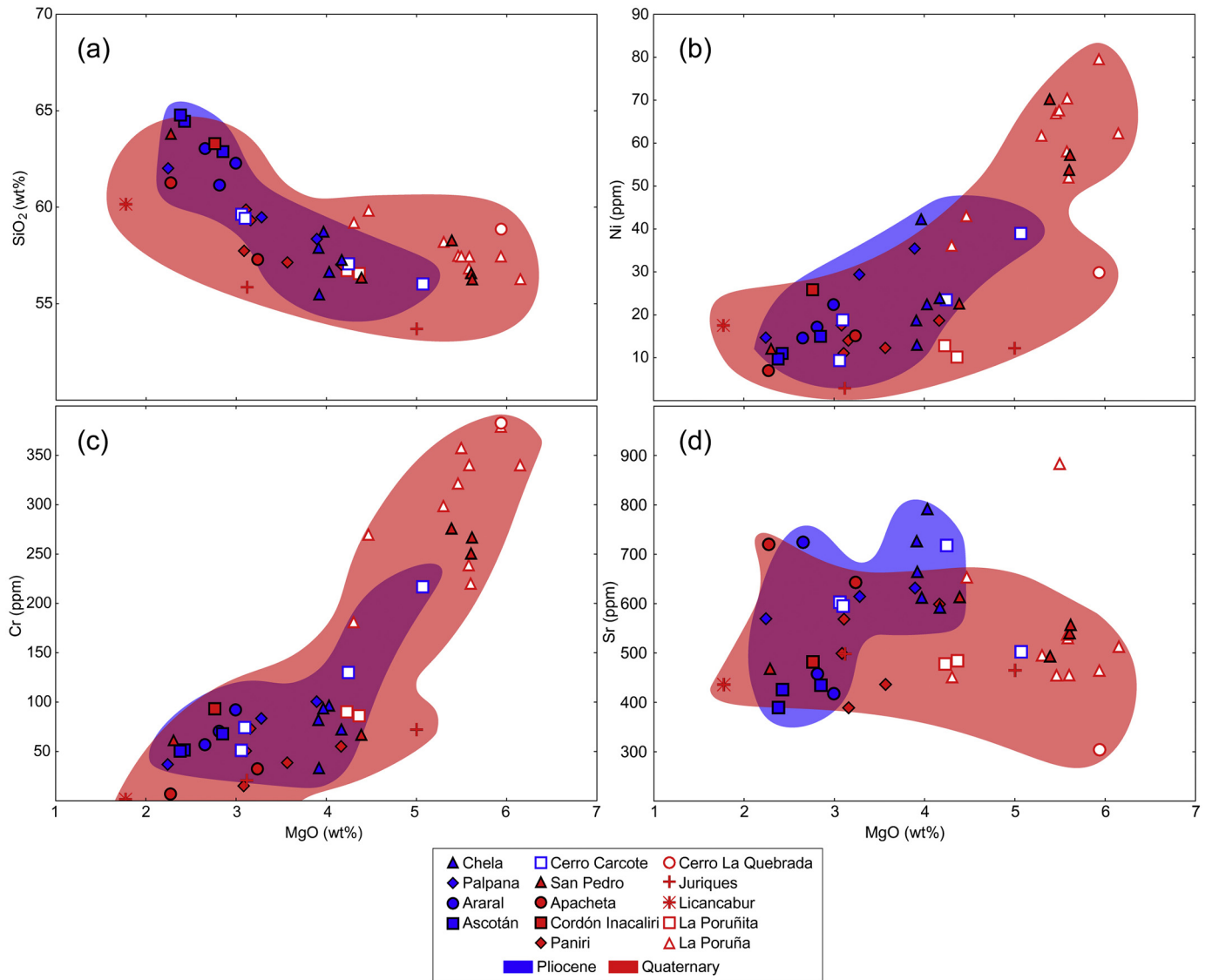


**Fig. 5.** Variation diagrams for the samples studied: (a) SiO<sub>2</sub> (wt%) vs. MgO (wt%). (b) Cr (ppm) vs. MgO (wt%). (c) Ni (ppm) vs. MgO (wt%). (d) Sr (ppm) vs. MgO (wt%). Note that the Pliocene samples (blue) tend to show slightly more restricted compositional ranges than the Quaternary samples (red).

HREE of the studied lavas may suggest a magmatic evolution dominated by low-pressure (garnet-free) processes (Fig. 6b; cf. Davidson et al., 2007; O'Callaghan and Francis, 1986). Indeed, low Sr/Y and La/Yb ratios support significant plagioclase fractionation and the absence of garnet or amphibole, in the source (Fig. 9c, d). Since garnet and amphibole are capable of controlling La/Yb ratios (Davidson et al., 2013), the Dy/Yb ratios versus silica is also plotted (Fig. 9e), as this ratio is sensitive to the presence of these phases. Low Dy/Yb ratios are indicative of the absence of garnet fractionation but may show evidence for the involvement of residual amphibole during differentiation (Fig. 9e), consistent with the main petrographic observations, as amphibole crystals appeared as minor phase in most samples (Section 4.1). Therefore, magma mixing, AFC or selective assimilation processes in a garnet-free differentiation environment at mid to upper crustal levels are required to fully explain most of the petrographic and geochemical characteristics of the studied samples.

As noted above, major and trace element concentrations and the radiogenic Sr and Nd isotopes support varied magmatic differentiation processes and variable degrees of crustal additions. Pliocene and Quaternary samples have wide ranges of e.g. SiO<sub>2</sub> (Fig. 4), MgO (Fig. 5), <sup>87</sup>Sr/<sup>86</sup>Sr and <sup>143</sup>Nd/<sup>144</sup>Nd ratios (Fig. 7), but these are relatively restricted when each volcano is examined individually. Thus, a remarkable compositional heterogeneity among the eruptive centers is recognized from the studied samples. We also note an apparent compositional variability with time, for example, in <sup>87</sup>Sr/<sup>86</sup>Sr and <sup>143</sup>Nd/<sup>144</sup>Nd ratios. Radiogenic isotope data for Pliocene samples leads to an expectation of a systematic increase of magma differentiation with time, however variable ratios are recognized in the Quaternary samples (Fig. 10). These compositional variations between the studied rocks is perhaps in part related to the spatial distribution of the volcanoes and may be linked to the projected APMB reservoir (Ward et al., 2014; Zandt et al., 2003). Thus, it is particularly relevant to discuss the influence of the APMB on the magmatic plumbing system

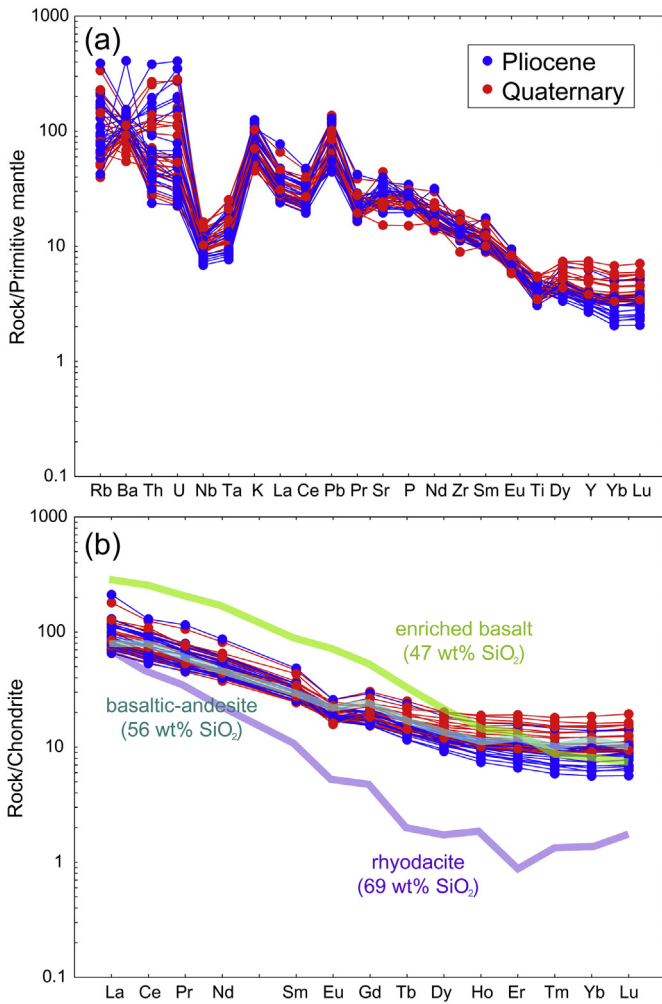


**Fig. 6.** Multi-element diagrams for analysed samples normalized to (a) primitive-mantle and (b) chondrite. (b) Chondrite-normalized rare earth element patterns of the studied rock samples are compared with the end-members suggested for the Central Andean magmatism (Blum-Oeste and Wörner, 2016), overlapping widely with the basaltic-andesite trend. Normalization values from McDonough and Sun (1995).

of the erupted mafic to intermediate lavas of our study (Figs. 1 and 2).

## 5.2. Spatiotemporal relation with the Altiplano-Puna Magma Body

To further understand the magmatic evolution of the studied mafic to intermediate Pliocene to Quaternary Andean volcanism at  $21^{\circ}10'–22^{\circ}50'S$ , the spatiotemporal framework of our samples relative to the APMB ought to be considered. A 3-D S-wave velocity model defines the dimensions of the APMB (Fig. 11), as of 4–30 km crustal depth and with the largest lateral extension of the partial melt body at a depth of 15 km (2.9 km/s velocity contour; Ward et al., 2014). The APMB is viewed as the source of the APVC ignimbrites (Zandt et al., 2003) and as a contaminant to the recent volcano plumbing systems (e.g. Godoy et al., 2019; González-Maurel et al., 2019; Taussi et al., 2019). A major ignimbrite pulse manifested locally at 8.3 Ma (e.g. Sifon ignimbrite, Salisbury et al., 2011) as well as the extensive Pliocene to Quaternary volcanism (Fig. 11) allow the assertion that the APMB has remained active over the last 8 Myr beneath this study area. We thus propose that the compositional variability observed here,

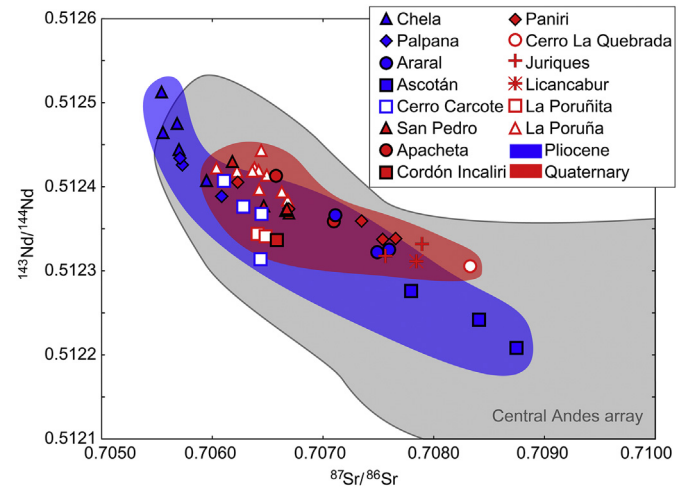


**Fig. 7.**  $^{143}\text{Nd}/^{144}\text{Nd}$  vs.  $^{87}\text{Sr}/^{86}\text{Sr}$  diagram for the studied samples. Grey field represents the isotope composition of Central Andes modern volcanism (Scott et al., 2018, and references therein). There is a strong correlation between  $^{87}\text{Sr}/^{86}\text{Sr}$  and  $^{143}\text{Nd}/^{144}\text{Nd}$  overall, with a differentiation trend more restricted to the Quaternary samples (red) relative to the Pliocene rocks (blue).

as larger variations are reflected against differentiation indexes (Section 5.1; e.g.  $\text{SiO}_2$ , MgO,  $^{87}\text{Sr}/^{86}\text{Sr}$ ; Figs. 7, 8 and 10), was influenced by the APMB reservoir. A systematic increase of the degree of crustal assimilation by ascending magmas as the vertical thickness of the APMB increased for the <2 Ma volcanism was proposed by Godoy et al. (2017), however we also consider the temporal variation prior to the <2 Ma volcanism as our samples span a longer time period. To evaluate the effect of variable isotope composition as a function of silica and assess the difference between volcanoes for mafic starting compositions, we consider baseline isotopic values of the least silicic sample at each volcano. Baseline isotopic compositions are thought to be inherited in the lower crustal MASH zone and are affected to a limited degree by crustal processes before eruption (Davidson et al., 1990; Freymuth et al., 2015; Hildreth and Moorbath, 1988). We have compiled geochemical data of the low silica (<64 wt%  $\text{SiO}_2$ ) lavas erupted in the western border of the APMB, dated from Pliocene to the present (Fig. 11), to determine the baseline isotopic values (Supplementary data 3, Table S3.1). Reference data in Fig. 12 (Supplementary data 3, Table S3.2) include Sr and Nd baseline radiogenic isotope ratios of twenty-seven (27) stratovolcanoes and monogenetic centers, including Uturuncu volcano (Bolivia) located in the centre of the current APMB. Pliocene and Quaternary volcanoes with the least evolved baseline values overlap with the borders of the APMB, whereas volcanoes located further inwards of this boundary show a more differentiated character (Fig. 12). This is further consistent with the variation in the petrography between the analysed samples in this work, as the olivine-pyroxene-bearing rocks are more common along the outer edge of the APMB (Table 2; Fig. 3). The olivine-pyroxene-bearing rocks generally show less evolved compositions compared with the pyroxene-bearing samples (Table 2), and remarkably La Poruña and San Pedro preserve the less evolved characteristics among the studied volcanoes in terms of compatible element contents (e.g. MgO, Cr, Ni; Fig. 5), which has been interpreted as local escape of mafic magma around the APMB (González-Maurel et al., 2019). As the differentiation processes such as magma mixing, AFC, or selective assimilation vary from volcano to volcano (Section 5.1), the

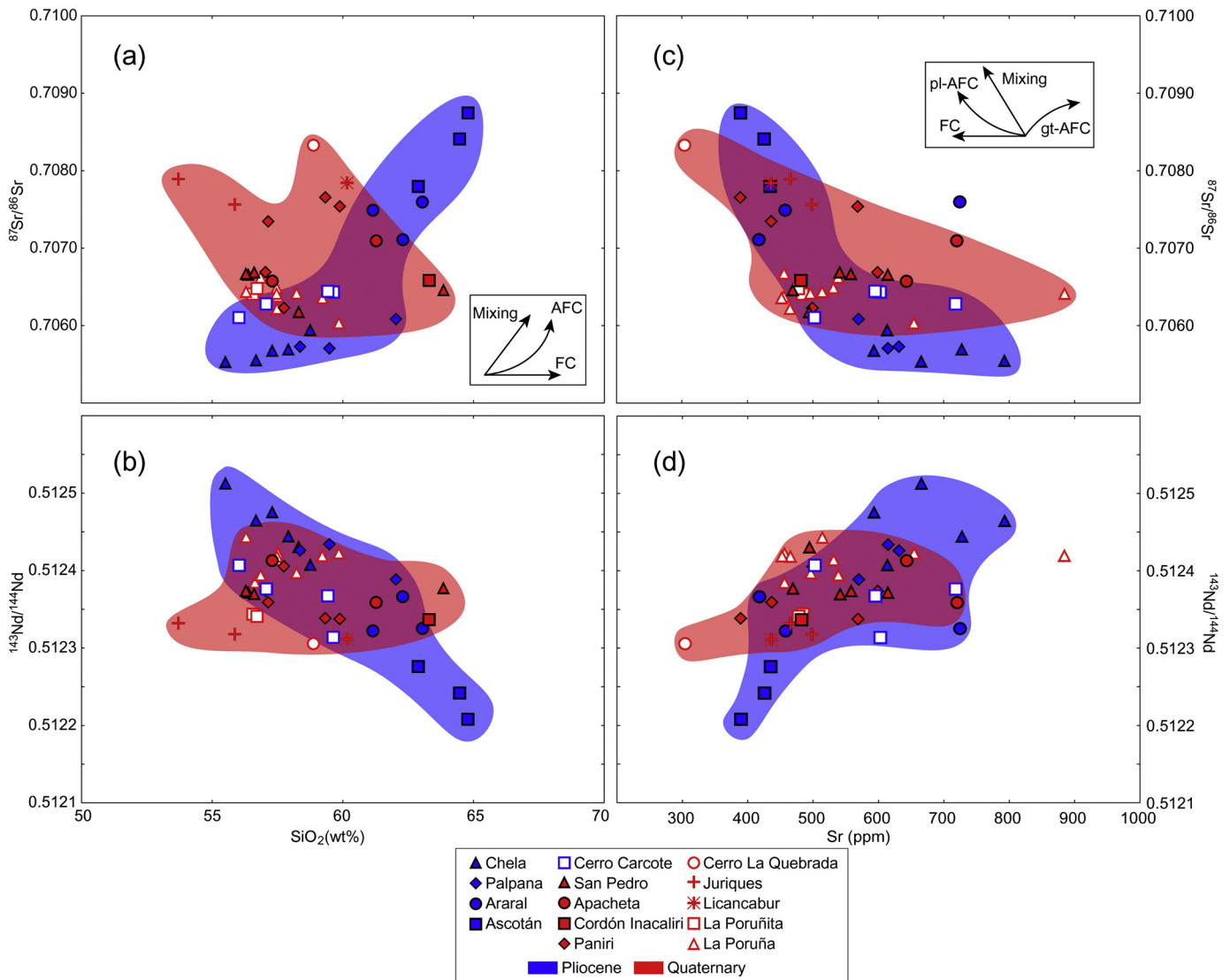


**Fig. 8.** <sup>87</sup>Sr/<sup>86</sup>Sr and <sup>143</sup>Nd/<sup>144</sup>Nd vs. SiO<sub>2</sub> (wt%) (a, b) and Sr (wt%) (c, d). Isotopic data demonstrate a large isotopic variation even in the less evolved melts. Inset shows the typical trends for: (a) mixing, assimilation and fractional crystallization (AFC), and fractional crystallization (FC) processes; and (c) mixing, plagioclase- and garnet-dominated assimilation and fractional crystallization (pl-AFC and gt-AFC, respectively), and fractional crystallization (FC) processes.

petrological variations seem also spatially related to the areal extent of the different velocity contours estimated for the APMB (Fig. 12). S-wave velocities indicate an increase in melt/fluid percentage from the margin to the centre of the partially molten body from ca. 4 vol% (3.2 km/s) to ca. 10 vol% (2.9 km/s), and up to 25 vol% (<1.9 km/s) (Ward et al., 2014; Fig. 12). Since portions of the APMB with low S-wave velocities (<2.9 km/s) contain higher amounts of melt and/or fluids (Ward et al., 2014), the ascending mafic magmas would be affected by high degrees of crustal assimilation and contamination. Therefore, such parental magmas passing through the APMB result in more evolved final compositions, whereas those erupted outside likely involved more restricted incorporation of derivative melts from the APMB (Figs. 11 and 12). These spatiotemporal variations of the baseline isotopic values into the S-wave velocity contours also lead us to suggest a possible APMB evolution through time. Most of the volcanoes located outside or within the 3.2 km/s contour share similar <sup>87</sup>Sr/<sup>86</sup>Sr and <sup>143</sup>Nd/<sup>144</sup>Nd

baseline ratios (Fig. 12), which may suggest fixed spatial limits for a relatively stationary APMB in time. Conversely, volcanoes constructed in the portions of low velocities (<2.9 km/s) exhibit more evolved but variable baseline compositions (Fig. 12), which we interpret as a reflection of continuous replenishment of magma from the mantle to the mid to upper crust that keep the APMB thermally active with contours of high partial melt potentially fluctuating in time. Judging on the location of Pliocene volcanoes (i.e. Araral and Ascotán) and younger volcanoes (e.g. Cerro del Azufre, Apacheta, Paniri) on the same velocity contour (Fig. 12a), and the elevated baseline Sr-isotope ratios in the Pliocene samples (Fig. 12b), the APMB contours with high percentages of partial melting (>10 vol%) may have been slightly more areally extensive in the Pliocene suggesting that these contours have shrunk since then.

Most petrological models include distinct levels of melt accumulation and melting in the continental crust where the basaltic-andesite magmas from the lower crust become

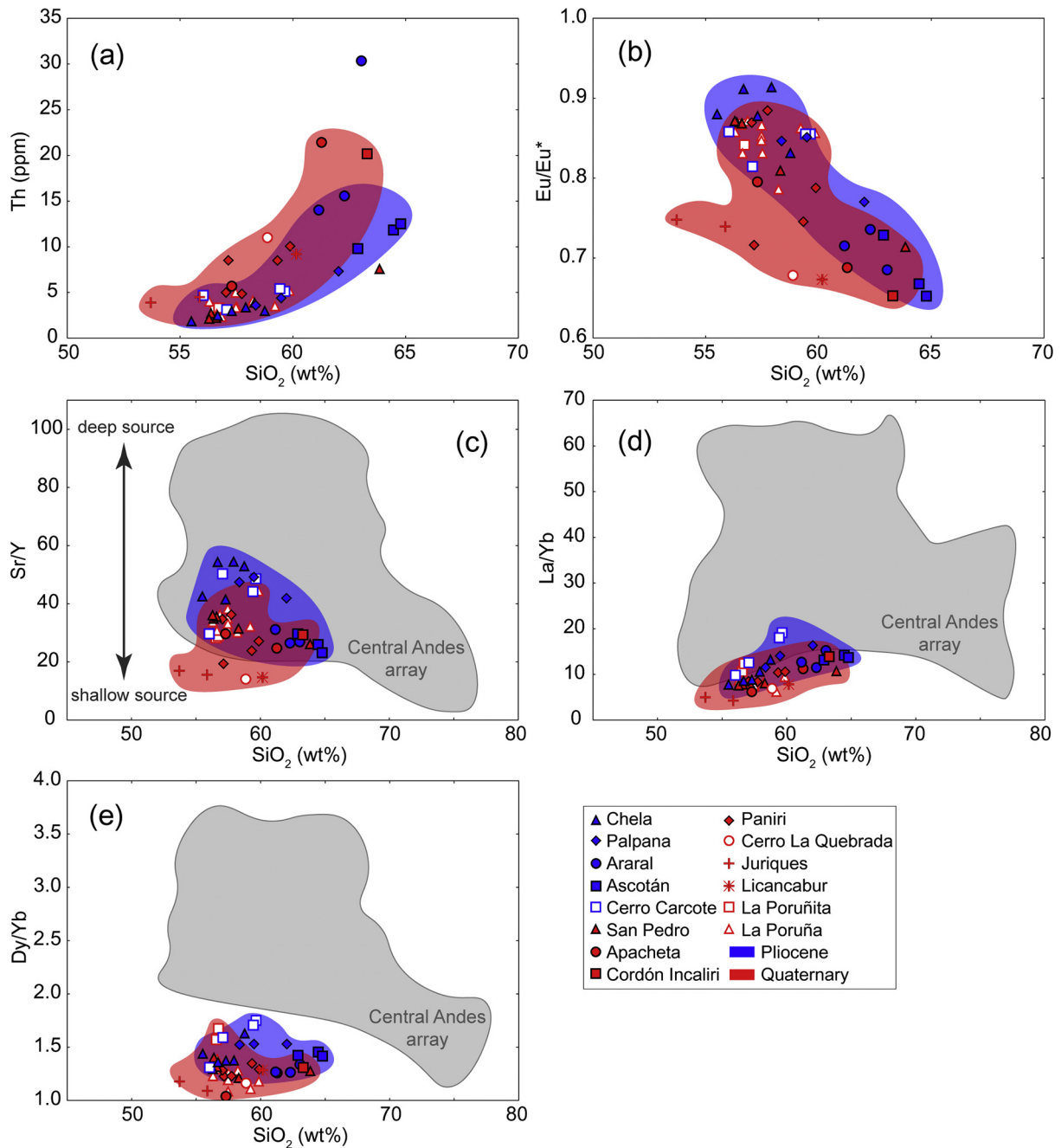


**Fig. 9.** Diagrams of (a) Th (ppm), (b) Eu/Eu\*, (c) Sr/Y, (d) La/Yb and (e) Dy/Yb vs. SiO<sub>2</sub> for the studied samples. Grey field represents the Central Andes array (Mamani et al., 2010). There is no significant temporal variation in these parameters between the analysed samples in this work, apart from that incompatible element ratios are slightly higher in the Pliocene samples in respect to the Quaternary samples, but still low enough to be related to mid-shallow crustal sources.

progressively more evolved at shallower depths (e.g. de Silva et al., 2006; Hildreth, 1981; Hildreth and Moorbath, 1988). The presence of the large APMB system implies a steady supply of basaltic-andesite melts into the crust that accumulate in an underplating zone beneath the APMB in the mid-crust (Perkins et al., 2016; Fig. 13). These dense mafic magmas in the underplating zone are not able to penetrate easily into the overlying low density APMB body and so tend to accumulate in the lower part of the reservoirs (e.g. Huber et al., 2009), however a larger thermal aureole surrounding the APMB is suggested by highest

S-wave seismic velocities of 2.9 to 3.2 km/s (Ward et al., 2014), which could represent a particularly ductile zone in the Central Andes that facilitated the movement of the ascending mafic magmas through a lined route and gave rise to the crustal melts of the uppermost crust. This implies that after the late Miocene initiation of the APMB, parental basaltic-andesite escape the lower crustal MASH zone and the APMB by lateral migration and ponding from where these finally escape by e.g. direct ascent (González-Maurel et al., 2019), likely exploiting upper crustal weakness zones (e.g. Giambiagi et al., 2016; Sellés and

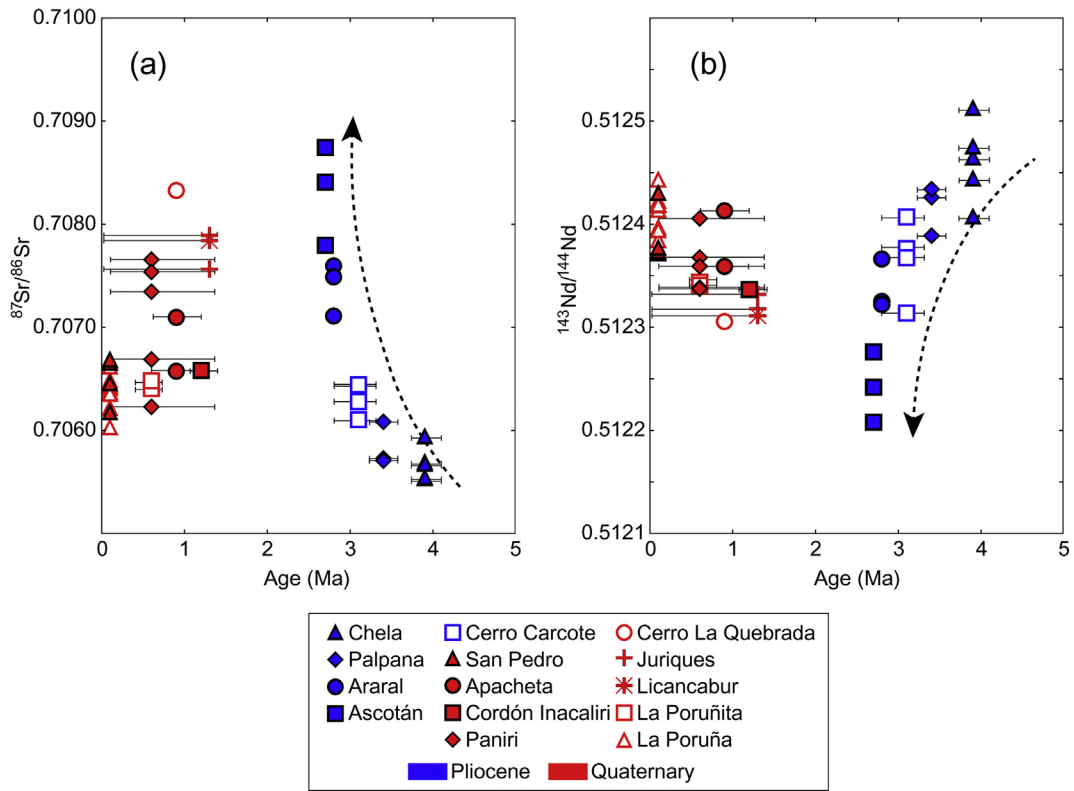


**Fig. 10.** (a)  $^{87}\text{Sr}/^{86}\text{Sr}$ , and (b)  $^{143}\text{Nd}/^{144}\text{Nd}$  vs. average Age (Ma) for the studied samples. Bars indicate maximum and minimum ages (Table 1). The Pliocene samples show a systematic increase and decrease of Sr and Nd isotope ratios through the time, respectively, whereas Quaternary samples show a scattered distribution.

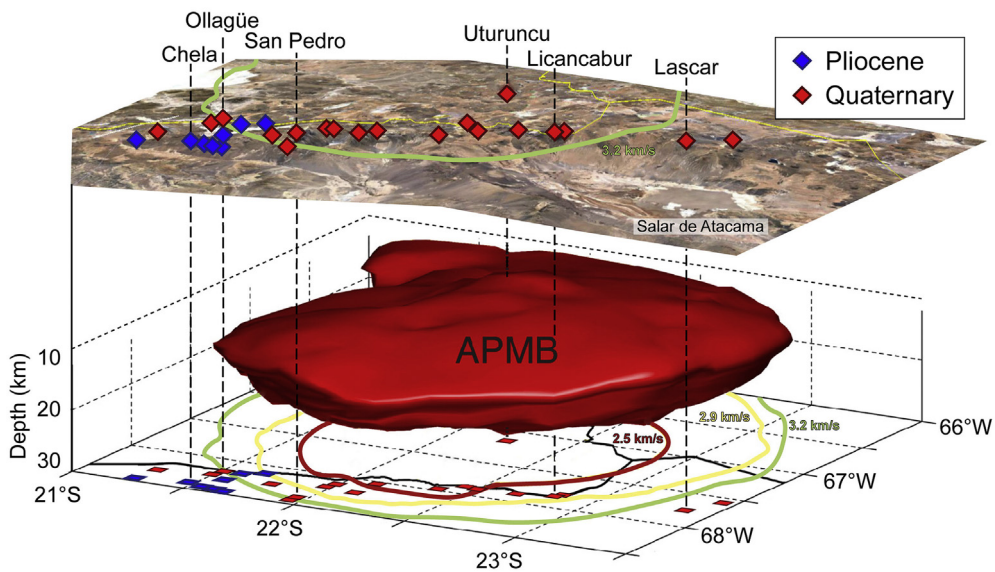


**Fig. 11.** 3-D volume model of the 2.9 km/s velocity contour (after Ward et al., 2014) showing the distribution of the Altiplano-Puna Magma Body and location of representative Pliocene to Quaternary volcanoes erupted above the partial melt anomaly.

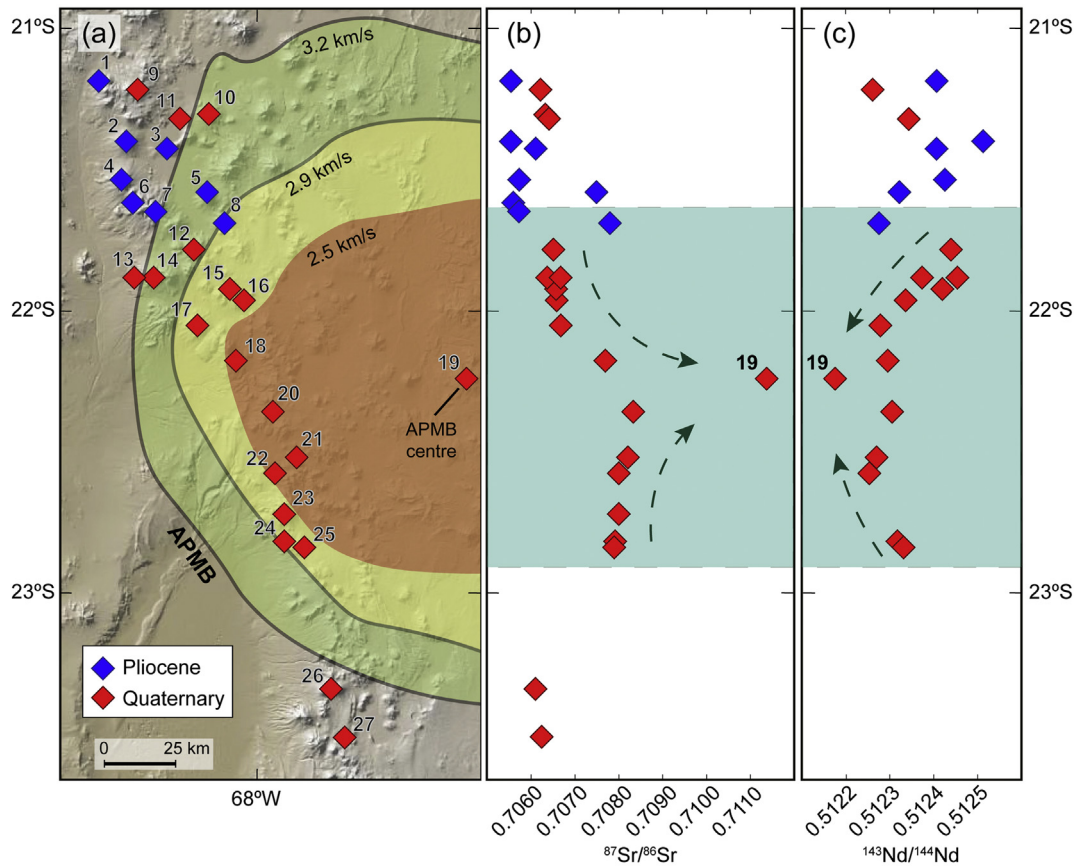


**Fig. 12.** (a) Global Multi-Resolution Topography (GMRT) image showing the location of the Pliocene and Quaternary volcanoes included in this study. Coloured areas indicate the estimated cross-section and extent of the APMB based on the joint ambient noise-receiver function inversion S-velocity model from Ward et al. (2014). (b, c) Baseline Sr (b) and Nd (c) isotopic values as a discriminant to assess the spatial and temporal evolution of the less silicic volcanism. Most of the Pliocene and Quaternary volcanoes outside or within the margin of the APMB show similar least evolved baseline values, whereas more evolved baseline values tend to appear further inwards of the melt body. Pliocene volcanoes: 1 – Miño, 2 – Chela, 3 – Cerro Carcote, 4 – Palpana, 5 – Araral, 6 – Cerro de las Cuevas, 7 – Cebollar and 8 – Ascotán. Quaternary volcanoes: 9 – Aucanquilcha, 10 – Ollagüe, 11 – La Poruña, 12 – Cerro del Azufre, 13 – La Poruña, 14 – San Pedro, 15 – Apacheta, 16 – Cordón Inacaliri, 17 – Paniri, 18 – Toconce, 19 – Uturuncu, 20 – Cerro La Quebrada, 21 – Putana, 22 – Colorado, 23 – Sairecabur, 24 – Licancabur, 25 – Juriques, 26 – Lascar and 27 – Cerro Overo. All data shown here are presented in Supplementary Material 3 (Table S3.2).

Gardeweg, 2017; Tibaldi et al., 2017) to migrate to the surface on the periphery of the APMB (Figs. 2 and 13). This model allows for variable degrees of parental magma-crust interaction with respect to their variable ascent routes either passing through or bypassing the APMB on their way to the surface, as the compositions of our mafic to intermediate magmas are strongly dependent on their eruption location relative to the larger APMB (Figs. 12 and 13).

## 6. Conclusions

The mafic to intermediate Pliocene to Quaternary volcanism that is concentrated on the western boundary of the Altiplano-Puna Volcanic Complex (between 21°10' to 22°50'S) occurs as lava flows from stratovolcanoes and as monogenetic cones. The investigated volcanic rocks are olivine and two-pyroxene phytic and range from medium-K to high-K calc-alkaline basaltic-andesite to dacite magmas with large compositional heterogeneity in major and trace element concentrations (e.g. SiO<sub>2</sub> = 53.2 to 63.2 wt%, MgO = 1.74 to 6.08 wt%, Cr = 2 to 382 ppm; Sr = 304 to 885 ppm) and in Sr and Nd isotopes (<sup>87</sup>Sr/<sup>86</sup>Sr = 0.7055–0.7087; <sup>143</sup>Nd/<sup>144</sup>Nd = 0.5122–0.5125). This compositional variability is explained by the interplay of parental basaltic-andesite magma assimilating continental crust or various

amounts of APMB derivate melts. Differentiation processes such as magma mixing, AFC, or selective assimilation occur at relatively low pressures in the middle to upper crust, but the development of these processes appears spatially variable from volcano to volcano. The least evolved eruptions occurred outside or just within the outer borders of the APMB, with volcanoes further inward from this border showing more differentiated overall geochemical and mineralogical features. The spatial isotope development of the magmatic system appears to be a useful indicator to evaluate the temporal evolution of mafic rocks in the region. The APMB remained thermally active since the late Miocene due to a steady replenishment of mafic melt from depth, represented by the investigated mafic to intermediate eruptives but may have slightly reduced its molten extent below the region at least since the Pliocene. The more evolved Pliocene samples possibly record a somewhat larger areal extent of the APMB contours with high percentages of partial melting (>10 vol%). Finally, we propose that the location of the less evolved magmas of the modern arc in the Altiplano-Puna Volcanic Complex is linked to the APMB borders where ascending parental basaltic-andesite magmas are diverted to avoid significant compositional modification prior to eruption. The study of these low-silica magmas thus offers a window into the 'parental' magma chambers that underplate the APMB and the state and size of the underlying larger APMB.

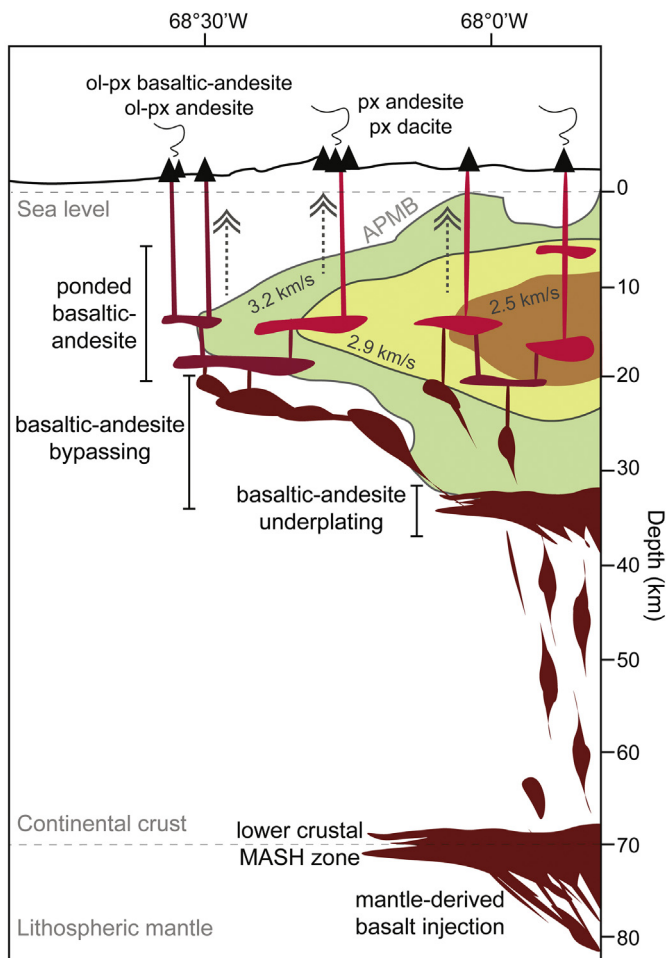


**Fig. 13.** Schematic cross-section of the continental crust showing the proposed magmatic evolution of the Pliocene to Quaternary least silicic magmas beneath the Altiplano-Puna Volcanic Complex province. Coloured areas indicate the estimated cross-section of the APMB based on the joint ambient noise-receiver function inversion S-velocity model from Ward et al. (2014). We suggest that mantle-derived magmas are injected beneath the APMB in an underplating zone after avoiding significant fractional crystallization in the MASH zone. A fraction of basaltic-andesite magma is diverted to the margins of the APMB, where it stalls, differentiates and fractionates in a mid to upper crustal plumbing system before ascent and eruption. Magmas that ascend through more central portions of the APMB, in turn, show higher rates of magma-crust interaction, reflecting higher uptake of APMB material during their journey.

## Acknowledgments

We thank Kerryn Gray and Fayroza Rawoot for their assistance during sample preparation and execution of XRF, ICP-MS and MC-ICP-MS procedures at UCT. We are grateful for the constructive comments that helped to significantly improve this manuscript from Dr. Nina Søager and an anonymous reviewer, and Dr. Andrew Kerr is thanked for editorial handling. This work has been funded by the Comisión Nacional de Investigación Científica y Tecnológica (CONICYT-PCHA/Doctorado Nacional/2015-21150403 to O.G.-M., and CONICYT-FONDAP 15090013/Centro de Excelencia en Geotermia de los Andes-Universidad de Chile to B.G.) and the Swedish Research Council (to V.R.T and F.M.D).

## Appendix A. Supplementary data

Supplementary data to this article can be found online at <https://doi.org/10.1016/j.lithos.2019.105162>.

## References

- Araya Vargas, J., Meqbel, N.M., Ritter, O., Brasse, H., Weckmann, U., Yáñez, G., Godoy, B., 2019. Fluid distribution in the Central Andes subduction zone imaged with magnetotellurics. *J. Geophys. Res. Solid Earth* 124. <https://doi.org/10.1029/2018JB016933>.
- Beck, S.L., Zandt, G., Myers, S.C., Wallace, T.C., Silver, P.G., Drake, L., 1996. Crustal-thickness variations in the Central Andes. *Geology* 24 (5), 407–410. <https://doi.org/10.1130/0091-7613>.
- Bertin, D., Amigo, A., 2019. Geología del volcán San Pedro, región de Antofagasta. Servicio Nacional de Geología y Minería, Carta Geológica de Chile, Serie Geología Básica, mapa escala 1:50.000 (Santiago, Chile).
- Bidart, N., 2014. Petrología y Geoquímica de Lavas Recientes, al Sureste del campo Geotermal del Tatio. Dissertation, B. Sc. Thesis. Universidad de Chile, Santiago, Chile.
- Blum-Oeste, M., Wörner, G., 2016. Central Andean magmatism can be constrained by three ubiquitous end-members. *Terra Nova* 28 (6), 434–440. <https://doi.org/10.1111/ter.12237>.
- Burns, D.H., de Silva, S.L., Tepley, F., Schmitt, A.K., Loewen, M.W., 2015. Recording the transition from flare-up to steady-state arc magmatism at the Purico-Chascon volcanic complex, northern Chile. *Earth Planet. Sci. Lett.* 422, 75–86. <https://doi.org/10.1016/j.epsl.2015.04.002>.
- Chmielowski, J., Zandt, G., Haberland, C., 1999. The central Andean Altiplano-Puna magma body. *Geophys. Res. Lett.* 26 (6), 783–786. <https://doi.org/10.1029/1999GL900078>.
- Comeau, M.J., Unsworth, M.J., Ticona, F., Sunagua, M., 2015. Magnetotelluric images of magma distribution beneath Volcán Uturuncu, Bolivia: implications for magma dynamics. *Geology* 43 (3), 243–246. <https://doi.org/10.1130/G36258.1>.
- Davidson, J.P., de Silva, S.L., 1995. Late cenozoic magmatism of the Bolivian Altiplano. *Contrib. Mineral. Petrol.* 119 (4), 387–408. <https://doi.org/10.1007/BF00286937>.
- Davidson, J.P., McMillan, N.J., Moorbath, S., Wörner, G., Harmon, R.S., López-Escobar, L., 1990. The Nevados de Payachata volcanic region (18°S/69°W, N. Chile) II. Evidence for widespread crustal involvement in Andean magmatism. *Contrib. Mineral. Petrol.* 105 (4), 412–432. <https://doi.org/10.1007/BF00286829>.
- Davidson, J.P., Harmon, R., Wörner, G., 1991. The source of central Andean magmas: some considerations. *Geol. Soc. Am. Spec. Pap.* 265, 233–243.
- Davidson, J.P., Turner, S., Handley, H., Macpherson, C., Dosseto, A., 2007. Amphibole “sponge” in arc crust? *Geology* 35 (9), 787–790. <https://doi.org/10.1130/G23637A.1>.
- Davidson, J.P., Turner, S., Plank, T., 2013. Dy/Dy\*: variations arising from mantle sources and petrogenetic processes. *J. Petrol.* 54 (3), 525–537. <https://doi.org/10.1093/petrology/egs076>.
- de Silva, S.L., 1989. Altiplano-Puna volcanic complex of the Central Andes. *Geology* 17 (12), 1102–1106. <https://doi.org/10.1130/0091-7613>.
- de Silva, S.L., Gosnold, W.D., 2007. Episodic construction of batholiths: insights from the spatiotemporal development of an ignimbrite flare-up. *J. Volcanol. Geotherm. Res.* 167 (1–4), 320–335. <https://doi.org/10.1016/j.jvolgeoes.2007.07.015>.
- de Silva, S.L., Kay, S.M., 2018. Turning up the heat: high-flux magmatism in the Central Andes. *Elements* 14 (4), 245–250. <https://doi.org/10.2138/gselements.14.4.245>.
- de Silva, S., Zandt, G., Trumbull, R., Viramonte, J., 2006. Large-scale silicic volcanism—the result of thermal maturation of the crust. *Adv. Geosci.* 1, 215–230. *Solid Earth (SE)*.
- del Potro, R., Diez, M., Blundy, J., Camacho, A.G., Gottsmann, J., 2013. Diapiric ascent of silicic magma beneath the Bolivian Altiplano. *Geophys. Res. Lett.* 40, 2044–2048. <https://doi.org/10.1002/grl.50493>.
- Delune, R., Blard, P.H., Martin, L.C.P., Nomade, S., Schlunegger, F., 2016. Longterm low latitude and high elevation cosmogenic <sup>3</sup>He production rate inferred from a 107 ka-old lava flow in northern Chile; 22°S–3400 m a.s.l. *Geochim. Cosmochim. Acta* 184, 71–87. <https://doi.org/10.1016/j.gca.2016.04.023>.
- DePaolo, D.J., 1981. Trace element and isotopic effects of combined wallrock assimilation and fractional crystallization. *Earth Planet. Sci. Lett.* 53 (2), 189–202. [https://doi.org/10.1016/0012-821X\(81\)90153-9](https://doi.org/10.1016/0012-821X(81)90153-9).
- Drew, S.T., Ducea, M.N., Schoenbohm, L.M., 2009. Mafic volcanism on the Puna Plateau, NW Argentina: Implications for lithospheric composition and evolution with an emphasis on lithospheric foundering. *Lithosphere* 1 (5), 305–318. <https://doi.org/10.1130/L54.1>.
- Figueroa, O., Déruelle, B., Demaiffe, D., 2009. Genesis of adakite-like lavas of Licancabur volcano (Chile–Bolivia, Central Andes). *C. R. Geoscience* 341 (4), 310–318. <https://doi.org/10.1016/j.crte.2008.11.008>.
- Francis, P.W., Hawkesworth, C.J., 1994. Late Cenozoic rates of magmatic activity in the Central Andes and their relationships to continental crust formation and thickening. *J. Geol. Soc. Lond.* 151 (5), 845–854. <https://doi.org/10.1144/gsjgs.151.5.845>.
- Freyer, H., Brandmeier, M., Wörner, G., 2015. The origin and crust/mantle mass balance of Central Andean ignimbrite magmatism constrained by oxygen and strontium isotopes and erupted volumes. *Contrib. Mineral. Petrol.* 169 (6), 58. <https://doi.org/10.1007/s00410-015-1152-5>.
- Frimmel, H.E., Zartman, R.E., Späth, A., 2001. Dating Neoproterozoic continental break-up in the Richtersveld Igneous complex, South Africa. *J. Geol.* 109 (4), 493–508. <https://doi.org/10.1086/320795>.
- Giambiagi, L., Alvarez, P., Spagnotto, S., 2016. Temporal variation of the stress field during the construction of the Central Andes: constraints from the volcanic arc region (22–26° S), Western Cordillera, Chile, during the last 20 Ma. *Tectonics* 35 (9), 2014–2033. <https://doi.org/10.1002/2016TC004201>.
- Godoy, B., Wörner, G., Le Roux, P., de Silva, S., Parada, M.A., Kojima, S., González-Maurel, O., Morata, D., Polanco, E., Martínez, P., 2017. Sr- and Nd- isotope variations along the Pleistocene San Pedro – Linzor volcanic chain, N. Chile: tracking the influence of the upper crustal Altiplano-Puna Magma Body. *J. Volcanol. Geotherm. Res.* 341, 172–186. <https://doi.org/10.1016/j.jvolgeoes.2017.05.030>.
- Godoy, B., Taussi, M., González-Maurel, O., Renzulli, A., Hernández-Prat, L., Le Roux, P., Morata, D., Menzies, A., 2019. Linking the mafic volcanism with the magmatic stages

- during the last 1 Ma in the main volcanic arc of the Altiplano-Puna Volcanic complex (Central Andes). *J. S. Am. Earth Sci.* 95, 102295. <https://doi.org/10.1016/j.jsames.2019.102295>.
- González-Maurel, O., Godoy, B., le Roux, P., Rodríguez, I., Marín, C., Menzies, A., Bertin, D., Morata, D., Vargas, M., 2019. Magmatic differentiation at La Poruña scoria cone, Central Andes, northern Chile: evidence for assimilation during turbulent ascent processes, and genetic links with mafic eruptions at adjacent San Pedro volcano. *Lithos* 338–339, 128–140.
- Harmon, R.S., Thorpe, R.S., Francis, P.W., 1981. Petrogenesis of Andean andesites from combined O–Sr isotope relationships. *Nature* 290 (5805), 396–399. <https://doi.org/10.1038/290396a0>.
- Harris, C., le Roux, P., Cochrane, R., Martin, L., Duncan, A.R., Marsh, J.S., le Roex, A.P., Class, C., 2015. The oxygen isotope composition of Karoo and Etendeka picrites: high  $\delta^{18}$ O. *Contrib. Mineral. Petrol.* 170, 1:1–24. <https://doi.org/10.1007/s00410-015-1164-1>.
- Hildreth, W., 1981. Gradients in silicic magma chambers: implications for lithospheric magmatism. *J. Geophys. Res. Solid Earth* 86 (B11), 10153–10192. <https://doi.org/10.1029/JB086iB11p10153>.
- Hildreth, W., Moorbath, S., 1988. Crustal contributions to arc magmatism in the Andes of Central Chile. *Contrib. Mineral. Petrol.* 98 (4), 455–489. <https://doi.org/10.1007/BF00372365>.
- Huber, C., Bachmann, O., Manga, M., 2009. Homogenization processes in silicic magma chambers by stirring and mushification (latent heat buffering). *Earth Planet. Sci. Lett.* 283, 38–47. <https://doi.org/10.1016/j.epsl.2009.03.029>.
- Irvine, T.N.J., Baragar, W.R.A.F., 1971. A guide to the chemical classification of the common volcanic rocks. *Can. J. Earth Sci.* 8 (5), 523–548. <https://doi.org/10.1139/e71-055>.
- Kay, S.M., Coira, B.L., Caffee, P.J., Chen, C.H., 2010. Regional chemical diversity, crustal and mantle sources and evolution of central Andean Puna plateau ignimbrites. *J. Volcanol. Geotherm. Res.* 198 (1), 81–111. <https://doi.org/10.1016/j.jvolgeores.2010.08.013>.
- Kelemen, P.B., Hanghøj, K., Greene, A.R., 2003. One view of the geochemistry of subduction-related magmatic arcs, with an emphasis on primitive andesite and lower crust. *Treat. Geochem.* 3, 593–659. <https://doi.org/10.1016/B0-08-043751-6/03035-8>.
- Kern, J.M., de Silva, S.L., Schmitt, A.K., Kaiser, J.F., Iriarte, A.R., Economos, R., 2016. Geochronological imaging of an episodically constructed subvolcanic batholith: U–Pb in zircon chronochimistry of the Altiplano-Puna Volcanic complex of the Central Andes. *Geosphere* 12 (4), 1054–1077. <https://doi.org/10.1130/GES01258.1>.
- Le Maitre, R.W., Bateman, P., Dudek, A., Keller, J., Lameyre, J., Le Bas, M.J., Sabine, P.A., Schmid, R., Sorensen, H., Strekeisen, A., Woolley, A.R., Zanettin, B., 1989. A Classification of Igneous Rocks and Glossary of Terms: Recommendations of the International Union of Geological Sciences, Subcommittee on the Systematics of Igneous Rocks (No. 552.3 CLA). *International Union of Geological Sciences*, p. 193.
- Mamani, M., Wörner, G., Sempere, T., 2010. Geochemical variations in igneous rocks of the Central Andean orocline (13°S to 18°S): tracking crustal thickening and magma generation through time and space. *Geol. Soc. Am. Bull.* 122 (1–2), 162–182. <https://doi.org/10.1130/B26538.1>.
- Marinovic, N., Lahsen, A., 1984. Hoja Calama. *Servicio Nacional de Geología y Minería, Carta Geológica de Chile, Serie Geología Básica* 58, 1 mapa escala 1:250.000 (Santiago, Chile).
- Mattioli, M., Renzulli, A., Menna, M., Holm, P.M., 2006. Rapid ascent and contamination of magmas through the thick crust of the CVZ (Andes, Ollagüe region): evidence from a nearly aphyric high-K andesite with skeletal olivines. *J. Volcanol. Geotherm. Res.* 158 (1–2), 87–105. <https://doi.org/10.1016/j.jvolgeores.2006.04.019>.
- McDonough, W.F., Sun, S.S., 1995. The composition of the earth. *Chem. Geol.* 120 (3–4), 223–253. [https://doi.org/10.1016/0009-2541\(94\)00140-4](https://doi.org/10.1016/0009-2541(94)00140-4).
- McKay, G.A., 1989. Partitioning of rare earth elements between major silicate minerals and basaltic melts. *Rev. Mineral. Geochem.* 21 (1), 45–77.
- Meade, F.C., Troll, V.R., Ellam, R.M., Freda, C., Font, L., Donaldson, C.H., Klonowska, I., 2014. Bimodal magmatism produced by progressively inhibited crustal assimilation. *Nat. Commun.* 5, 4199. <https://doi.org/10.1038/ncomms5199>.
- O’Callaghan, L.J., Francis, P.W., 1986. Volcanological and petrological evolution of San Pedro volcano, Provincia El Loa, North Chile. *J. Geol. Soc. Lond.* 143, 275–286. <https://doi.org/10.1144/gsjgs.143.2.0275>.
- Peccerillo, A., Taylor, S.R., 1976. Geochemistry of Eocene calc-alkaline volcanic rocks from the Kastamonu area, northern Turkey. *Contrib. Mineral. Petrol.* 58 (1), 63–81. <https://doi.org/10.1007/BF00384745>.
- Perkins, J.P., Ward, K.M., de Silva, S.L., Zandt, G., Beck, S.L., Finnegan, N.J., 2016. Surface uplift in the Central Andes driven by growth of the Altiplano Puna Magma body. *Nat. Commun.* 7, 13185. <https://doi.org/10.1038/ncomms13185>.
- Salisbury, M.J., Jicha, B.R., de Silva, S.L., Singer, B.S., Jiménez, N.C., Ort, M.H., 2011.  $^{40}\text{Ar}/^{39}\text{Ar}$  chronostratigraphy of Altiplano-Puna volcanic complex ignimbrites reveals the development of a major magmatic province. *Bulletin* 123 (5–6), 821–840. <https://doi.org/10.1130/B30280.1>.
- Scott, E.M., Allen, M.B., Macpherson, C.G., McCaffrey, K.J., Davidson, J.P., Saville, C., Ducea, M.N., 2018. Andean surface uplift constrained by radiogenic isotopes of arc lavas. *Nat. Commun.* 9 (1), 969. <https://doi.org/10.1038/s41467-018-03173-4>.
- Seelenfreund, A., Fonseca, E., Llona, F., Lera, L., Sinclair, C., Rees, C., 2009. Geochemical analysis of vitreous rocks exploited during the formative period in the Atacama region, northern Chile. *Archaeometry* 51 (1), 1–25. <https://doi.org/10.1111/j.1475-4754.2008.00386.x>.
- Sellés, D., Gardeweg, M., 2017. *Geología del área Ascotán-Cerro Inacaliri, región de Antofagasta. Servicio Nacional de Geología y Minería, Carta Geológica de Chile, Serie Geología Básica*. vol. 190, p. 73 (1 mapa escala 1:100.000. Santiago, Chile).
- Streck, M.J., 2008. Mineral textures and zoning as evidence for open system processes. *Rev. Mineral. Geochem.* 69, 595–622. <https://doi.org/10.2138/rmg.2008.69.15>.
- Taussi, M., Godoy, B., Piscaglia, F., Morata, D., Agostini, S., le Roux, P., González-Maurel, O., Gallmeyer, G., Menzies, A., Renzulli, A., 2019. The upper crustal magma plumbing system of the Pleistocene Apacheta-Aguilucho Volcanic complex area (Altiplano-Puna, northern Chile) as inferred from the erupted lavas and their enclaves. *J. Volcanol. Geotherm. Res.* 373, 179–198. <https://doi.org/10.1016/j.jvolgeores.2019.01.021>.
- Taylor, S.R., McLennan, S.M., 1988. The significance of the rare earths in geochemistry and cosmochemistry. *Handbook Phys. Chem. Rare Earths* 11, 485–578. [https://doi.org/10.1016/S0168-1273\(88\)11011-8](https://doi.org/10.1016/S0168-1273(88)11011-8).
- Tibaldi, A., Bonali, F.L., Corazzato, C., 2017. Structural control on volcanoes and magma paths from local-to orogen-scale: the Central Andes case. *Tectonophysics* 699, 16–41. <https://doi.org/10.1016/j.tecto.2017.01.005>.
- Troll, V.R., Chadwick, J.P., Ellam, R.M., Mc Donnell, S., Emelex, C.H., Meighan, I.G., 2005. Sr and Nd isotope evidence for successive crustal contamination of Slieve Gullion ring-dyke magmas, Co. Armagh, Ireland. *Geol. Mag.* 142 (6), 659–668. <https://doi.org/10.1017/S0016756805001068>.
- Ward, K.M., Zandt, G., Beck, S.L., Christensen, D.H., McFarlin, H., 2014. Seismic imaging of the magmatic underpinnings beneath the Altiplano-Puna volcanic complex from the joint inversion of surface wave dispersion and receiver functions. *Earth Planet. Sci. Lett.* 404, 43–53. <https://doi.org/10.1016/j.epsl.2014.07.022>.
- Wörner, G., Hammerschmidt, K., Henjes-Kunst, F., Lezaun, J., Wilke, H., 2000. Geochronology ( $^{40}\text{Ar}/^{39}\text{Ar}$ , K–Ar and He-exposure ages) of Cenozoic magmatic rocks from northern Chile (18–22°S): implications for magmatism and tectonic evolution of the Central Andes. *Rev. Geol. Chile* 27 (2), 205–240. <https://doi.org/10.4067/S0716-0208200000200004>.
- Wörner, G., Mamani, M., Blum-Oeste, M., 2018. Magmatism in the Central Andes. *Elements* 14 (4), 237–244. <https://doi.org/10.2138/gselements.14.4.237>.
- Zandt, G., Leidig, M., Chmielowski, J., Baumont, D., Yuan, X., 2003. Seismic detection and characterization of the Altiplano-Puna magma body, Central Andes. *Pure Appl. Geophys.* 160 (3), 789–807. <https://doi.org/10.1007/PL00012557>.
- Zen, E.A., 1986. Aluminum enrichment in silicate melts by fractional crystallization: some mineralogical and petrographic constraints. *Journal of Petrology* 27 (5), 1095–1117. <https://doi.org/10.1093/ptrology/27.5.1095>.